Received: 17 March 2023 | Revised: 21 June 2023 | Accepted: 10 July 2023

DOI: 10.1002/qj.4534

Quarterly Journal of the Royal Meteorological Society RMetS

RESEARCH ARTICLE

Changes of tropical gravity waves and the quasi-biennial oscillation in storm-resolving simulations of idealized global warming

Henning Franke[1,2] | **Peter Preusse**[3] | **Marco Giorgetta**[1]

[1]Max Planck Institute for Meteorology, Hamburg, Germany

[2]International Max Planck Research School on Earth System Modelling, Max Planck Institute for Meteorology, Hamburg, Germany

[3]Institut für Energie- und Klimaforschung – Stratosphäre (IEK-7), Forschungszentrum Jülich GmbH, Jülich, Germany

Correspondence
Henning Franke, Max Planck Institute for Meteorology, Bundesstraße 53, 20146 Hamburg, Germany.
Email: henning.franke@mpimet.mpg.de

Funding information
Bundesministerium für Bildung und Forschung, Grant/Award Number: 2019215178

Gravity waves generated by tropical deep convection contribute significantly to driving the downward propagation of the quasi-biennial oscillation (QBO). However, it is currently uncertain how gravity waves and their interaction with the QBO, and thus the QBO itself, will respond to a warming climate. Previous work showed that this uncertainty is a consequence of the parametrization of gravity waves employed in conventional general circulation models. In this study, we therefore perform short explicit simulations of the QBO for different idealized climate states with the model ICON-A in a deep convection-permitting set-up, which means that neither a parametrization of convection nor a parametrization of gravity waves is employed and that the QBO is entirely driven by explicitly resolved waves. Thereby, our simulations allow us to provide a very first direct estimate of how tropical gravity waves and the QBO may change in a warming climate. We found that the gravity wave momentum flux in the lower stratosphere that is relevant for the QBO increases substantially in the warmer climate states and shifts towards faster zonal phase speeds. As a consequence, the downward propagation of the QBO accelerates and the magnitude of the QBO jets in the upper QBO domain increases in the warmer climate states. Thus, our work builds an important first step towards a more comprehensive assessment of potential QBO changes using global storm-resolving models.

KEYWORDS

gravity waves, global storm-resolving models, global warming, QBO, tropical stratosphere, wave–mean flow interactions

1 | INTRODUCTION

The quasi-biennial oscillation (QBO) is the dominant mode of interannual variability in the equatorial stratosphere and is characterized by the descent of alternating easterly and westerly wind jets with a period of ~28 months (Baldwin *et al.*, 2001). It has been shown that the QBO has a profound impact on stratospheric circulation and transport (Baldwin *et al.*, 2001, and references therein) and that it influences tropical

convection (Giorgetta *et al.*, 1999; Collimore *et al.*, 2003), the Madden–Julian oscillation (Yoo and Son, 2016; Son *et al.*, 2017), and extratropical surface variability (Anstey and Shepherd, 2014). Thus, it is important to understand if and how the QBO may change in a warming climate, and several studies have attempted to address this problem using conventional general circulation models (GCMs) (Giorgetta and Doege, 2005; Kawatani *et al.*, 2011; Kawatani *et al.*, 2012; Kawatani and Hamilton, 2013; Schirber *et al.*, 2015; Butchart *et al.*, 2020; Richter *et al.*, 2020). However, their results disagree with each other, and results of single studies have been partly inconclusive. Schirber *et al.* (2015) and Richter *et al.* (2020) showed that this is largely due to the inherent uncertainties in the gravity wave (GW) parametrizations that conventional GCMs have to employ in order to simulate a reasonable QBO. In this work, therefore, we use a high-resolution GCM that explicitly resolves rather than parametrizes GWs and deep convection to provide a more reliable estimate of how the GW momentum flux (GWMF) and the QBO may change in a warming climate.

To understand how the QBO may change in a warming climate one first has to understand how the processes that control its downward propagation change in a warming climate. The first process is the interaction of the QBO jets with a broad spectrum of upward-propagating equatorial waves, which drives the QBO's descent by depositing zonal momentum in the shear zones of the QBO jets. The wave spectrum driving the QBO ranges from planetary-scale waves, most prominently equatorial Kelvin, equatorial Rossby, and mixed Rossby–GWs, down to small-scale GWs with horizontal wavelengths of $\mathcal{O}$(10 km). All of these waves are predominantly generated by different modes of tropical deep convection. The second process controlling the QBO is the vertical advection of zonal momentum by the general tropical upwelling associated with the rising branch of the Brewer–Dobson circulation (BDC). The tropical upwelling usually opposes the wave-driven downward propagation of the QBO jets, and thus slows it down (Baldwin *et al.*, 2001; Anstey *et al.*, 2022).

Based on model projections, it is now well established that the tropical upwelling will increase in a warmer climate (e.g., Butchart *et al.*, 2006; Hardiman *et al.*, 2014), and Shepherd and McLandress (2011) have presented a robust mechanism explaining this. They argue that the warming-induced strengthening of the subtropical jets pushes the critical levels of the waves driving the BDC upwards, allowing more wave activity to penetrate into the lower stratosphere, which accelerates the BDC. It has been shown that this increase in tropical upwelling acts to slow down the downward propagation of the QBO and to reduce its amplitude, especially in the lower stratosphere (Kawatani *et al.*, 2011; Kawatani *et al.*, 2012; Kawatani and Hamilton, 2013; Richter *et al.*, 2020). Kawatani and Hamilton (2013) further identified a decreasing QBO amplitude in the lower stratosphere in the observational record, which they also attribute to an increase in tropical upwelling. The link between tropical upwelling and the downward propagation speed of the QBO can also operate in the opposite direction, as Giorgetta and Doege (2005) and Watanabe and Kawatani (2012) showed that a decrease in tropical upwelling results in a faster QBO downward propagation. Thus, the impact of an increased tropical upwelling onto the QBO is relatively well understood and established, and it can be found robustly across models.

In contrast, the response of the resolved and parametrized wave forcing of the QBO to a warming climate is much more uncertain and is strongly model dependent (Richter *et al.*, 2020). Even though there seems to be a clear tendency towards an increase in the total QBO wave forcing, the magnitude of this change differs strongly across studies and models (see Giorgetta and Doege, 2005; Kawatani *et al.*, 2011; Richter *et al.*, 2020). Depending on whether the increase in the total QBO wave forcing will outweigh the increase in tropical upwelling or not, the QBO will either accelerate or decelerate in a warming climate; that is, its period will shorten or lengthen respectively. Consequently, some studies show a deceleration of the QBO (Kawatani *et al.*, 2011; Kawatani and Hamilton, 2013) and others show an acceleration of the QBO (Giorgetta and Doege, 2005). More recently, Richter *et al.* (2020) analyzed the response of the QBO to idealized warmer climates across 11 GCMs in the framework of the Stratosphere–troposphere Processes and their Role in Climate (SPARC) Quasi-Biennial Oscillation initiative (QBOi) project (Butchart *et al.*, 2018). They also found that the QBO response to this warming is uncertain, with some models showing the QBO to speed up, some models showing it to slow down, and some models showing it to break down. The same lack of agreement in projections of the QBO period was found across Coupled Model Intercomparison Project phase 5 (Kawatani and Hamilton, 2013) and Coupled Model Intercomparison Project phase 6 (CMIP6) (Butchart *et al.*, 2020) models. Building up on the recent disruptions of the QBO in 2016 (Osprey *et al.*, 2016; Coy *et al.*, 2017) and 2019–2020 (Kang and Chun, 2021), Anstey *et al.* (2021) further suggest that the QBO may additionally become more susceptible to disruptions in a warming climate. Thus, the answer to the question of how the QBO may change in a warming climate ultimately remains uncertain.

Schirber *et al.* (2015) and Richter *et al.* (2020) showed that a large part of this uncertainty in QBO projections by conventional GCMs stems from their GW parametrizations. The reasons for this are manifold. First

of all, the tropical GWMF is still poorly constrained by observations, even for current-day climate conditions. Therefore, GW parametrizations are often tuned towards a realistic current-day climate (Orr *et al.*, 2010; Garcia *et al.*, 2017), and this tuning set-up may not be valid in different climate states. Additionally, a substantial number of current state-of-the-art GCMs still use GW parametrizations that employ a fixed GW source spectrum. Thus, they are by design not able to respond to changes in GW sources due to a warming climate (Richter *et al.*, 2020). However, Richter *et al.* (2020) also showed that those models employing a GW parametrization coupled to the convective sources of GWs disagree with regard to changes in GWMF in the lower stratosphere, even in the sign of change. Additional uncertainty stems from the fact that convection itself is also parametrized in conventional GCMs.

Obviously, it is necessary to reduce the uncertainty in the projections of tropical GWMF in the first place in order to ultimately reduce the uncertainty in QBO projections. One possibility to achieve a more realistic projection of the tropical GWMF is the explicit simulation of non-orographic GWs in global high-resolution models. However, because of the immense computational costs associated with this kind of simulation, they have so far been only feasible at resolutions that fail to resolve substantial parts of the GW spectrum and which still require the parametrization of deep convection (Watanabe *et al.*, 2005; Kawatani *et al.*, 2010a; Kawatani *et al.*, 2010b; Kawatani *et al.*, 2011; Kawatani *et al.*, 2012; Holt *et al.*, 2016). Only one study explicitly investigated how the GWMF in the lower stratosphere could change in a warming climate (Watanabe *et al.*, 2005).

The continuous increase in computational power now finally allows for global simulations at horizontal resolutions at which deep convection and GWs with horizontal wavelengths of $\mathcal{O}(10)$ km become explicitly resolved and no longer need to be parametrized. The corresponding models are commonly referred to as global storm-resolving models (GSRMs). It has been shown that GSRMs are able to reproduce an overall realistic spectrum and global distribution of convectively generated GWs (Müller *et al.*, 2018; Stephan *et al.*, 2019a), even though substantial intermodel differences in the GWMF remain (Stephan *et al.*, 2019b) and the resolution at which GSRMs resolve the GW spectrum truly sufficiently remains unclear (Lane and Knievel, 2005; Polichtchouk *et al.*, 2021). Despite these limitations, GSRMs offer great potential to study how the tropical GWMF may change in a warming climate in general and how this may affect the QBO in particular.

In this study, we thus use the GSRM ICON-A (Zängl *et al.*, 2015) to try to answer the two key research questions that emerge from the current uncertainty in QBO projections for a warming climate:

1. *How does the spectrum of convectively generated GWs in the Tropics, as well as their associated GWMF, change in a warming climate?* This question is motivated by the substantial uncertainty of projections of tropical GWMF due to the inherent uncertainties of GW parametrizations and will be addressed in Section 4.
2. *How does the QBO change in a warming climate if its GW forcing is simulated explicitly?* This question is motivated by the uncertainty in QBO projections due to the uncertainty in GWMF projections and will be answered in Section 5.

2 | METHODS

2.1 | ICON-A model configuration

The numerical experiments of this study have been conducted with the global atmosphere-only GCM ICON-A (Giorgetta *et al.*, 2018), which employs a non-hydrostatic dynamical core (Zängl *et al.*, 2015). ICON-A is formulated on an unstructured triangular horizontal grid derived from a spherical icosahedron, which is obtained by projecting an icosahedron onto the sphere formed by its vertices (Wan *et al.*, 2013). To allow for the intended direct simulation of deep convection, the simulations of this study make use of the R2B9 grid, which has an equivalent horizontal resolution of $\Delta x \approx 5$ km (see Giorgetta *et al.*, 2018, Tab. 1) and which has been shown to allow for a reasonable simulation of deep convection (Hohenegger *et al.*, 2020) and GW spectra (Müller *et al.*, 2018; Stephan *et al.*, 2019a). The vertical grid of ICON-A used in this study is a terrain-following hybrid sigma height grid (Leuenberger *et al.*, 2010) consisting of 191 levels up to a height of 83 km. The resulting vertical grid spacing is $\Delta z \approx 350$ m in the tropopause region and $\Delta z \approx 560$ m in the stratopause region. Previous investigations indicate that this vertical resolution is sufficient to capture the main features of the wave–mean flow interactions that drive the QBO (Giorgetta *et al.*, 2006; Geller *et al.*, 2016a). In order to make simulations at this very high resolution feasible, the ICON-A model has been adapted to run on graphics processing unit (GPU) architectures (Giorgetta *et al.*, 2022), which is used in this study in version rc2.6.5.

As our model set-up is intended to allow for the direct simulation of deep convection and convectively generated GWs, neither a parametrization of convection nor a parametrization of non-orographic GW drag is employed. Additionally, the parametrization of subgrid-scale orographic GW drag is switched off in order to ensure that

the entire wave forcing in our simulations originates from explicitly resolved waves only. To avoid reflection of resolved waves at the model top, as well as to reduce other numerical artifacts stemming from the upper model boundary, a Rayleigh damping on the vertical wind w is applied (Klemp *et al.*, 2008), which starts at 50 km and so does not directly affect the QBO or the stratospheric dynamics in general. Vertical diffusion of heat, momentum, and tracers is parametrized using the total turbulent energy scheme of Mauritsen *et al.* (2007) in the set-up described in Pithan *et al.* (2015). In contrast to the baseline version of ICON-A presented in Giorgetta *et al.* (2018), the GPU-enabled ICON-A version used in this study employs the RTE + RRTMGP radiation scheme (Pincus *et al.*, 2019). To ensure numerical stability and to suppress numerical noise, ICON-A applies a combination of horizontal diffusion and divergence damping. The horizontal diffusion is set up as a second-order Smagorinsky diffusion on potential temperature and velocity combined with a fourth-order background diffusion on velocity. The approach for the divergence damping used in this study is a combined second-order and fourth-order damping acting on the three-dimensional velocity divergence. A more detailed description of the set-up of the GPU-enabled ICON-A used in this study can be found in Giorgetta *et al.* (2022).

Giorgetta *et al.* (2022) have shown that the ICON-A set-up described is capable of simulating the downward progression of the QBO jets with time due to wave–mean flow interactions in the shear zones of the QBO. However, it must be noted that the downward progression of the QBO in their simulation was about three times faster than in the fifth-generation European Centre for Medium-Range Weather Forecasts Atmospheric Reanalysis (ERA5).

2.2 | Experimental set-up

The experimental design of our study closely follows the protocol of the QBOi experiments 2, 3, and 4 (Butchart *et al.*, 2018), which have been analyzed in Richter *et al.* (2020). Accordingly, we have defined three idealized climate states, which are prescribed to ICON-A:

- *Ref climate*: A reference climate with 1988–2007 monthly mean sea-surface temperatures (SST) and sea-ice concentrations (SICs) stemming from the CMIP6 input datasets (Durack and Taylor, 2019). The concentrations of carbon dioxide (CO_2) and other radiative trace gases have been specified to their 1988–2007 mean values, also based on their CMIP6 input datasets (Meinshausen *et al.*, 2017), which gives a CO_2 concentration of 365.59 ppm.
- *+2 K climate*: A double-CO_2 climate, in which the CO_2 concentration is doubled compared with the reference climate and a globally uniform SST increase of +2 K compared with the reference climate is employed. Despite the changes in SST and CO_2 concentration, SICs are kept at their reference climate values. Concentrations of other radiative trace gases are also kept at their reference climate values.
- *+4 K climate*: A quadruple-CO_2 climate, in which the CO_2 concentration is quadrupled compared with the reference climate and a globally uniform SST increase of +4 K compared with the reference climate is employed. Despite the changes in SST and CO_2 concentration, SICs are kept at their reference climate values. Concentrations of other radiative trace gases are also kept at their reference climate values.

Based on the results of Deser *et al.* (2015), we do not expect the constant SICs to have a significant influence on the tropical atmosphere, including the QBO. In all three climate states, the solar forcing is fixed at its 2002 conditions. Furthermore, ozone is not simulated interactively within our model set-up; instead, three-dimensional ozone concentrations (Hegglin *et al.*, 2016) are prescribed as their 2002 monthly mean values in all three climate states. Consequently, the QBO–ozone feedback, as well as potential feedbacks stemming from projected ozone changes in the future, is not recognized in our study. Thereby, our experimental set-up guarantees that any change in the QBO and in stratospheric GWMF is solely attributable to the changes employed in CO_2 concentrations and SST. We chose the year 2002 as a reference year based on the QBOi experimental protocol (Butchart *et al.*, 2018), which argues that the El Niño–Southern Oscillation and the Pacific decadal oscillation were in a neutral state in 2002 and, furthermore, no explosive volcanic eruptions occurred. Nevertheless, it should be noted that the 2002 ozone amounts are impacted by a Southern Hemisphere sudden stratospheric warming (e.g., Shepherd *et al.*, 2005).

For each idealized climate state we performed two experiments in order to account for the role of the QBO phase. The first set of experiments was initialized on April 1, 2004, 0000 UTC, when the QBO was in a phase of westerly shear (experiments Ref-west, +2 K-west, and +4 K-west), and the second set of experiments was initialized on April 1, 2005, 0000 UTC, when the QBO was in a phase of easterly shear (experiments Ref-east, +2 K-east, and +4 K-east). In both cases the model was initialized from the European Centre for Medium-Range Weather

Forecasts' Integrated Forecasting System operational analysis for the corresponding date and time. The zonal wind profiles in the tropical stratosphere at the two initialization time steps are shown in Figure 1. Each experiment was integrated for 45 days, and instantaneous output was written every 2 hr. The first 15 days out of the total simulated 45 days per experiment are considered as spin-up, which has been found to be reasonable based on the temporal evolution of thermodynamic properties of the tropical atmosphere (see Supporting Information B). Therefore, only the last 30 days of each experiment are used for analysis. An overview of all simulations performed for this study can be found in Table 1.

2.3 | Postprocessing of model output

The majority of the diagnostics used in our study require their input data to be provided on a regular latitude–longitude grid and on geometric height coordinates (see Section 2.4). Additionally, disk space constraints made it impossible to store the raw output of all experiments, making it necessary to reduce the amount of data. Therefore, we performed a distance-weighted average remapping of the raw model output coming from the triangular R2B9 grid to a regular n256 Gaussian grid (grid spacing of ∼39 km near the Equator) based on the 13 nearest neighbors. In the vertical, we have interpolated the raw model output coming from terrain-following hybrid sigma height levels to the geometric height levels corresponding to the sigma height levels over ocean. Since the model levels transition from sigma height levels to constant height levels above 22.5 km on the whole globe, no vertical interpolation was performed above this height. This means that the largest part of the tropical stratosphere is not influenced by the vertical interpolation. All analysis in our study is based on the postprocessed data.

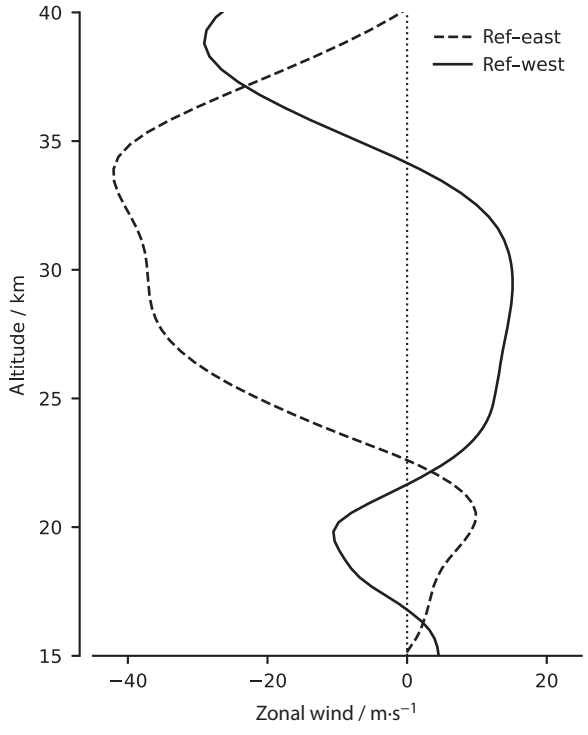

FIGURE 1 The 5° S – 5° N zonal mean zonal wind profiles in the stratosphere at model initialization.

2.4 | Diagnostics

2.4.1 | Wave generation by deep convection

To investigate the generation of GW by deep convection in the tropical troposphere, we make use of the analysis developed by Müller *et al.* (2018) and analyze the in-cloud vertical velocity w_{cld} and the in-cloud latent heating rate $Q_{\mathrm{lat,cld}}$ within 15° S and 15° N. Additionally, we analyze the cloud fraction Γ_{cld}, which is defined as the amount of cloudy grid cells per altitude level divided by the total amount of grid cells within 15° S and 15° N. At any altitude, a grid cell is defined as cloudy if its total cloud condensate mass mixing ratio q_{T} exceeds 0.1 g kg^{-1}.

Furthermore, we calculate the zonal wave number power spectra of total precipitation (pr) in the Tropics, which are a wide-used proxy of tropical tropospheric wave activity (see, e.g., Müller *et al.*, 2018; Polichtchouk *et al.*, 2021). The spectral power $P_{\mathrm{pr}}(k)$ of precipitation estimates its variance as a function of zonal wave number k and is given by

$$P_{\mathrm{pr}}(k) = F_{\mathrm{pr}}(k)\tilde{F}_{\mathrm{pr}}(k), \tag{1}$$

where $F_{\mathrm{pr}}(k)$ denotes the complex Fourier transform of precipitation calculated by a fast Fourier transformation in longitude and $\tilde{F}_{\mathrm{pr}}(k)$ denotes its complex conjugate. We have calculated the spectra for each time step and along each latitude between 15° S and 15° N.

Spectral characteristics of the stratospheric wave field in the Tropics are analogously analyzed by calculating the co-spectral power $P_{uw}(k)$ of the zonal wind u and the vertical wind w as

$$P_{uw}(k) = \Re(F_{\mathrm{u}}(k)\tilde{F}_{\mathrm{w}}(k)), \tag{2}$$

where $F_u(k)$ denotes the complex Fourier transform of u, $\tilde{F}_w(k)$ denotes the complex conjugate of the complex Fourier transform of w, and $\Re()$ denotes the real part of a complex number. The product of $P_{uw}(k)$ and air density ρ may then be interpreted as the zonal momentum flux

TABLE 1 Set-up of all simulations performed.

Experiment	SST change	CO_2 change	Initialization
Ref-west	—	—	April 1, 2004
+2 K-west	+2 K	Doubling	April 1, 2004
+4 K-west	+4 K	Quadrupling	April 1, 2004
Ref-east	—	—	April 1, 2005
+2 K-east	+2 K	Doubling	April 1, 2005
+4 K-east	+4 K	Quadrupling	April 1, 2005

Abbreviations: CO_2, carbon dioxide; SST, sea-surface temperature.

spectrum; that is, the spectrum of the vertical flux of zonal momentum $\rho u'w'$, where the prime denotes departure from the zonal mean background wind.

2.4.2 | Stratospheric gravity wave field

Our output interval of 2 hr is clearly too coarse to temporally resolve the shortest GWs that are spatially resolved by the postprocessed data, which can have periods as short as ~17 min. Therefore, neither the GW pseudomomentum flux nor GW phase speed spectra can be diagnosed using the classical spectral approach via Fourier analysis in space and time. Instead, we decided to use the small-volume few-wave decomposition technique (S3D, Lehmann *et al.*, 2012), which is suited to diagnose the characteristics of the stratospheric GWs as well as their associated momentum fluxes at individual time steps. S3D has the additional advantage that it provides local information of GWs, since GW characteristics are given as function of physical space instead of spectral space. It has already been used by Stephan et al. (2019a) and Stephan et al. (2019b) to diagnose GW characteristics in global storm-resolving simulations.

Technically, S3D performs three-dimensional sinusoidal fits on subsets of perturbation temperature and vertical wind to calculate the local wave vector and amplitude in each subset. In the following, the individual steps of the S3D algorithm as employed in our study are explained in more detail.

1. *Vertical regridding*. The postprocessed output fields of temperature T, zonal wind u, meridional wind v, vertical wind w, and pressure p are linearly regridded to an evenly spaced height coordinate with a vertical spacing of 500 m starting at a height of 1.5 km.
2. *Split up into background and perturbation component*. Each vertically regridded variable ϑ is split into a background component ϑ_0 and a perturbation component ϑ' by performing a fast Fourier transformation in the zonal direction, followed by a split at zonal wave number 18 (zonal wavelength $\lambda_x \approx 2{,}220$ km near the Equator). Thus, the background component contains most planetary waves, as well as large-scale gradients, whereas the perturbation component retains mostly GW signals, at least in the stratosphere. In accordance with Strube *et al.* (2020), we have used a cut-off wave number of 18, which also removes synoptic Rossby waves present in the lower stratosphere. Furthermore, the background component is smoothed using a Savitzky–Golay filter (Savitzky and Golay, 1964) in latitude based on third-order polynomials over 5° latitude.
3. *Cuboid subsets*. The three-dimensional perturbation temperature within our analysis domain between ~38° S and ~38° N is divided into subsets of cuboids with a size of 330 × 330 km^2 in the horizontal and 10 km in the vertical. The chosen cuboid size agrees with Lehmann *et al.* (2012) and ensures that we can theoretically identify waves with horizontal wavelengths λ_h between ~80 km and ~3,300 km and vertical wavelengths λ_z between ~1 km and ~35 km. However, wavelengths at the lower and upper edge of these ranges are not reliably identifiable (see S3D step 5). Within our analysis domain, the cuboid centers are placed every ~3.51° in the zonal direction and every ~3.16° in the meridional direction so that neighboring cuboids within the deep Tropics do not overlap. In the vertical direction, the cuboids are centered every 500 m between 20 and 40 km, so that only the very bottom of the lowest cuboid is located below the tropopause whereas the top of the highest cuboid is still located well below the sponge layer. We chose this very high vertical sampling interval to accurately resolve the vertical gradient of GWMF.
4. *Initial three-dimensional sinusoidal fit*. Within each cuboid separately, three subsequent three-dimensional sinusoidal fits are performed to the temperature perturbations to determine the wave component j which minimizes the remaining variance based on the least squares method. After the optimal solution for wave

component j has been determined, it is subtracted from the perturbation temperature and the fit for wave component $j+1$ is performed. In this way, we derive the amplitude $\hat{T}_j$ and the three-dimensional wave vector $\boldsymbol{k}_j = (k_j, l_j, m_j)$ of all three wave components j.

5. *Rejecting unreliable fits*. As described in detail in Stephan et al. (2019b), fits resulting in a wavelength λ_ζ much larger than the cuboid size Δ_ζ of a given direction ζ must be considered as unreliable. Within our study, fits resulting in $\lambda_h > 3.5\Delta_h$ or $\lambda_z > 3\Delta_z$ are considered as unreliable and are therefore rejected from further analysis.
6. *Three-dimensional refit*. Using the previously determined wave vector $\boldsymbol{k}_j$ of each wave component j as a priori information, a three-dimensional sinusoidal refit is performed to the same initial temperature perturbations as in S3D step 2 inside each cuboid for each wave component j. This refit helps to achieve a more reliable estimation of the wave amplitude $\hat{T}_j$ of each wave component j.
7. *Derive wave quantities*. Using the smoothed background fields determined in step 2, additional wave quantities such as GWMF are derived from the wave vector $\boldsymbol{k}_j$ and the amplitude $\hat{T}_j$. According to linear wave theory, the GWMF $\boldsymbol{F}_{\mathrm{GW},j} = \left(F^{(x)}_{\mathrm{GW},j}, F^{(y)}_{\mathrm{GW},j}\right)$ of each wave component j can be estimated as (cf. Ern *et al.*, 2004; Ern *et al.*, 2017)

$$\boldsymbol{F}_{\mathrm{GW},j} = \frac{\rho_0}{2}\frac{(k_j, l_j)}{m_j}\left(\frac{g}{N_0}\right)^2\left(\frac{\hat{T}_j}{T_0}\right)^2, \tag{3}$$

where ρ_0 denotes the background density, g denotes the gravitational acceleration, N_0 denotes the background buoyancy frequency, and T_0 denotes the background temperature. The assumption of upward propagating waves removes the ambiguity in the horizontal propagation direction of a wave. The total GWMF, $\boldsymbol{F}_{\mathrm{GW}} = \left(F^{(x)}_{\mathrm{GW}}, F^{(y)}_{\mathrm{GW}}\right)$, is calculated as

$$\boldsymbol{F}_{\mathrm{GW}} = \sum_{j=0}^{2} \boldsymbol{F}_{\mathrm{GW},j}. \tag{4}$$

Information on how the S3D algorithm calculates the ground-based zonal phase speed is given in the Supporting Information.

3 | CHANGES IN MEAN CLIMATE

3.1 | Temperatures and zonal winds

Using experiment +4 K-east as an example, Figure 2a,c shows that ICON-A reliably simulates the basic atmospheric response to an increase in SST and CO_2 concentration. Compared with the reference climate, tropospheric temperatures increase substantially in +4 K-east, with the strongest increase in the upper tropical troposphere, whereas stratospheric temperatures decrease. Consistent with thermal wind balance, the subtropical jets in both hemispheres strengthen accordingly and shift upward and poleward. In contrast, zonal winds in the lower troposphere change little, especially in the Tropics. These fundamental changes also occur in the other warming experiments, with the magnitude of change scaling with the magnitude of imposed idealized warming (not shown).

As shown by the 15° S–15° N mean temperature profile in Figure 2b, the tropospheric warming leads to an upward shift of the tropical tropopause by about 1 km in the +2 K climates and by about 2 km in the +4 K climates. Since the QBO vanishes near the tropopause layer, the upward shift of the tropopause would have a direct impact on the vertical extent of the QBO domain. The 15° S–15° N mean zonal winds, shown in Figure 2d, are generally weak in the troposphere in all experiments. In the upper troposphere, above an altitude of 10 km, the 15° S–15° N mean zonal winds have a clear westerly anomaly in the warmer climate states. Therefore, we do expect the idealized warming to have an impact on vertical wave propagation via critical-level filtering within the upper troposphere.

Within the tropical troposphere, neither winds nor temperatures depend significantly on the QBO phase in all three climate states. This is different in the stratosphere, where the temperatures are directly influenced by adiabatic heating or cooling associated with the secondary meridional circulation of the QBO. Consequently, temperatures in the lower stratosphere in the westerly shear experiments are higher by about 2 K than in their corresponding easterly shear experiments.

3.2 | Tropical precipitation

Precipitation is a widely used proxy to assess the characteristics of tropical deep convection as the main trigger for tropical waves of all scales (e.g., Müller *et al.*, 2018; Polichtchouk *et al.*, 2021). This is based on the facts that, in the Tropics, the majority of precipitation is produced by deep convection and that the total precipitation is proportional to the net latent heat release of a deep-convective cloud, which is the main mechanism by which deep convection generates GWs (see Fritts and Alexander, 2003, and reference therein). Consequently, it is important that our storm-resolving set-up of ICON-A simulates a realistic spatio-temporal distribution of tropical precipitation in order to generate a realistic tropical wave spectrum.

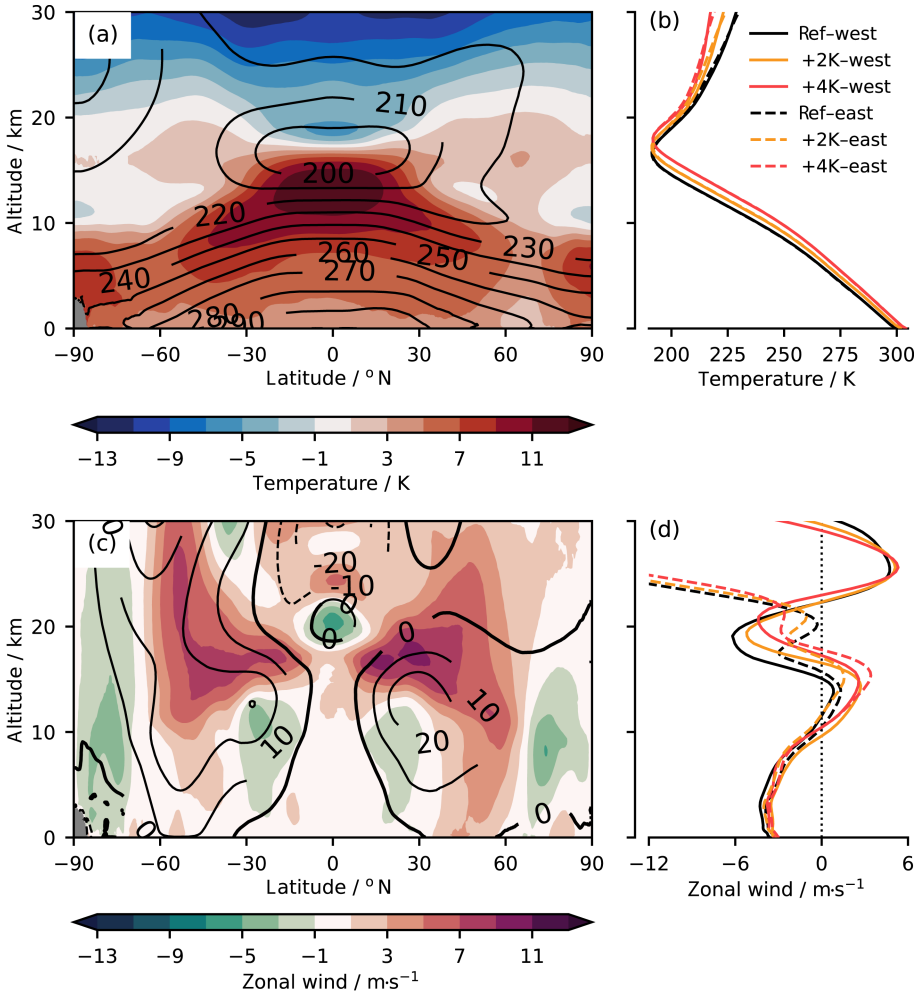

FIGURE 2 Difference in (a) zonal mean temperature (colour shading) and (c) zonal mean zonal wind (colour shading) between experiment +4 K-east and experiment Ref-east averaged over the last 30 simulation days. Contour lines indicate (a) the zonal mean temperature and (c) the zonal mean zonal wind of experiment Ref-east. Panels (b) and (d) show the 15° S–15° N zonal mean (b) temperature and (d) zonal wind profiles of all experiments averaged over the last 30 simulation days. [Colour figure can be viewed at wileyonlinelibrary.com]

As shown by Figure 3a, the zonal mean distribution of precipitation in our simulations agrees reasonably well with that of the satellite-based observational Integrated Multi-satellite Retrievals for the Global Precipitation Measurement (IMERG) dataset (Huffman *et al.*, 2019) and the ERA5 product (Hersbach *et al.*, 2020), even though there are some obvious differences. Most notably, all of our simulations show a pronounced double intertropical convergence zone (ITCZ) bias with a spurious southern hemispheric ITCZ, resulting in too strong a precipitation between ~1° S and ~5° S that is outside the range of internal variability for both ERA5 (years 1988–2007) and IMERG (years 2001–2007). As a further manifestation of the double ITCZ bias, equatorial precipitation is too weak in our simulations compared with IMERG and ERA5. However, it should be noted that the double ITCZ bias is not specific to ICON-A but instead is one of the most common biases in GCMs, regardless of whether they parametrize convection (Fiedler *et al.*, 2020; Tian and Dong, 2020) or simulate it explicitly (Stevens *et al.*, 2019, see their Fig. 5). Figure 3b shows that the relative occurrence frequency of precipitation in our simulations matches the one in IMERG reasonably well, whereas ERA5 fails to produce a realistic amount of strong precipitation and overestimates weak precipitation. This finding highlights the added value of explicit convection in simulating tropical precipitation realistically compared with parametrized convection, such as in ERA5. It further shows that ICON-A is capable of simulating intense smaller scale deep convection, albeit too much compared with IMERG, which is an important source of small-scale GWs (Fritts and Alexander, 2003). These findings are also represented by the large values of zonal variance in our simulations compared with ERA5 and IMERG (see Table 2).

In the warmer climate states, the characteristics of tropical precipitation change compared with their corresponding reference climate states. As shown in Table 2, both the tropical mean (i.e., 15° S to 15° N mean) precipitation and its zonal variance increase overall robustly in the warmer climate states. Apart from experiment +2 K-west, the warming-induced anomalies in tropical mean precipitation are larger than its interannual variability during the analysis time span in IMERG (years 2001–2007) and

TABLE 2 The 15° S to 15° N mean precipitation statistics of our experiments, the satellite-based observational product Integrated Multi-satellite Retrievals for the Global Precipitation Measurement (IMERG), and the fifth-generation European Centre for Medium-Range Weather Forecasts Atmospheric Reanalysis (ERA5) product averaged over the analysis time span from April 16 to May 15.

Experiment	$\overline{pr}$/mm·day^{-1}	$\Delta\overline{pr}$/%	σ^2_{pr}/mm^2·day^{-2}	$\Delta\,\sigma^2_{pr}$/%
Ref-west	5.07	—	1138.48	—
+2 K-west	5.12	+0.92	1364.52	+19.85
+4 K-west	5.53	+9.00	1668.00	+46.51
Ref-east	4.77	—	1075.39	—
+2 K-east	5.27	+10.50	1396.28	+29.84
+4 K-east	5.49	+14.96	1651.71	+53.59
ERA5	4.78±0.20	—	185.38±26.79	—
IMERG	4.85±0.14	—	975.79±54.12	—

Note: $\overline{pr}$: 15° S to 15° N mean precipitation rate. $\Delta\overline{pr}$: relative difference of 15° S to 15° N mean precipitation rate between the warmer climate states and their corresponding reference climate state. σ^2_{pr}: 15° S to 15° N mean zonal variance of precipitation rate. $\Delta\sigma^2_{pr}$: relative difference of 15° S to 15° N mean zonal variance of precipitation rate between the warmer climate states and their corresponding reference climate. To highlight the internal variability of tropical precipitation during our Atmospheric Modelling Intercomparison Project (AMIP) reference period (1988–2007 for ERA5, 2001–2007 for IMERG), the average value of these periods and the standard deviation (±) are given.

ERA5 (years 1988–2007), as represented by their relative sample standard deviation of 2.9% and 4.2% respectively. Therefore, we conclude that, at least for an idealized exaggerated warming of +4 K, the changes in precipitation amount can be attributed to the imposed warming with high confidence. Nevertheless, it must be noted that the quantitative estimates of changes in tropical mean precipitation in our short simulations are likely uncertain due to internal variability. This is highlighted by the fact that even between both reference experiments (Ref-east and Ref-west) the tropical mean precipitation differs by up to 6%. Additionally, Figure 3a shows that warming-induced precipitation anomalies occur non-uniformly across latitudes. On a local scale, even for an idealized warming of +4 K the amount of precipitation change lies within the range of interannual variability in both ERA5 (years 1988–2007) and IMERG (years 2001–2007).

In contrast to the overall precipitation amount, warming-induced changes in precipitation intensity are much more robust across our simulations, as shown in Figure 3b. In the warmer climates we see a clear increase in the occurrence frequency of strong precipitation, whereas the occurrence frequency of weak precipitation decreases. Thereby, the increase in strong precipitation scales approximately exponentially with the amount of idealized warming. These findings hold for both the westerly and the easterly shear experiments, and there are no significant quantitative differences between both sets of experiments. Recalling the fact that tropical precipitation is a reasonable proxy for the generation of tropical waves by deep convection, we expect the warming-induced changes in precipitation to have a notable impact on the tropical wave field.

4 | CHANGES IN TROPICAL GRAVITY WAVES

4.1 | Wave generation by deep convection

The warming-induced changes in the characteristics of tropical precipitation clearly suggest a more vigorous generation of tropical waves, which means that the waves get stronger or their generation occurs more frequently or over a wider area. In order to investigate in more detail how the generation mechanisms of tropical waves in our simulations change, we analyze the in-cloud latent heating and the in-cloud vertical velocity as established by Müller *et al.* (2018) (see Section 2.4.1). Here, the in-cloud latent heating serves as a direct proxy of the thermal forcing of GWs by latent heat release in deep convective storms (Fritts and Alexander, 2003). Similarly, the in-cloud vertical velocity serves as a proxy of the mechanical forcing of GWs by the oscillations of convective updrafts around their level of neutral buoyancy at the cloud top (Fritts and Alexander, 2003). However, Fritts and Alexander (2003) also point out that the thermal and mechanical forcing of GWs should not be considered as two distinct processes but rather act in a coupled manner due to the inherent coupling between the latent heat release and the vertical velocity in a deep convective cloud.

As shown in Figure 4a,b, for both the westerly and the easterly shear experiments the overall in-cloud latent heating increases in the warmer climate states, which is in agreement with the overall increase in tropical precipitation (see Section 3.2). The increase in latent heating is most

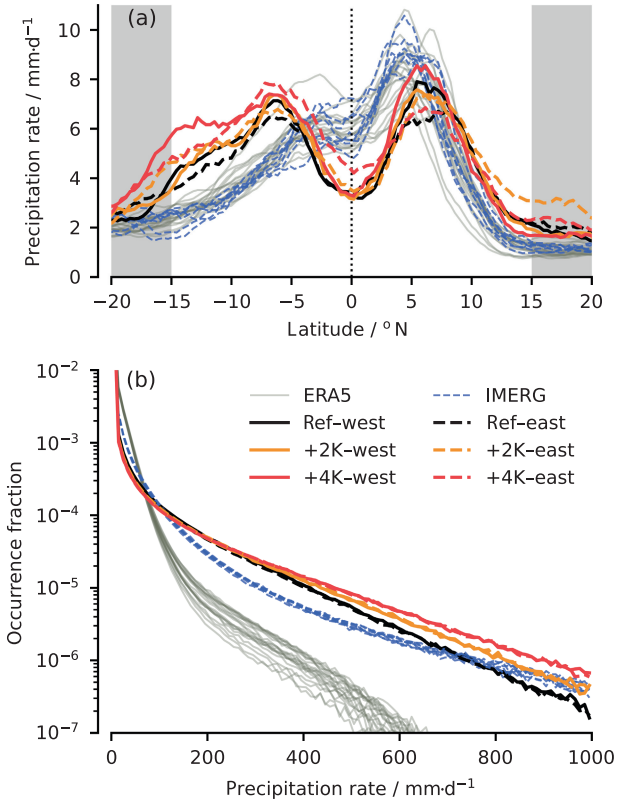

FIGURE 3 Key tropical precipitation characteristics of our experiments, the satellite-based observational product Integrated Multi-satellite Retrievals for the Global Precipitation Measurement (IMERG), and the fifth-generation European Centre for Medium-Range Weather Forecasts Atmospheric Reanalysis (ERA5) product during the analysis time span from April 16 to May 15: (a) zonal mean precipitation as a function of latitude and (b) probability density function of precipitation between 15° S and 15° N, both based on two-hourly mean precipitation rates. To highlight the internal variability of tropical precipitation during our Atmospheric Modelling Intercomparison Project reference period (1988–2007), individual years in that period are plotted for ERA5 and IMERG (only 2001–2007 available). Gray bars in (a) denote areas outside of 15° S and 15° N, which are not used for calculating the probability density function in (b). [Colour figure can be viewed at wileyonlinelibrary.com]

obvious for the strong and very strong convective events as represented by the 90th percentile and the 99th percentile of in-cloud latent heating respectively. There, the absolute value of the peak latent heating between 6 km and 11 km increases by about 4.5–8.5% for the +2 K climates and by about 12–22% for the +4 K, which is a clear indication of more intense convection. Based on these results, we therefore expect the generation of stronger thermally forced GWs; that is, GWs with a larger amplitude.

Figure 4c,d shows the in-cloud vertical velocity w_{cld} as a proxy for the mechanical forcing of GWs. It is immediately evident that in the warmer climate states the mean w_{cld} and the 90th and 99th percentiles of w_{cld} increase compared with their corresponding reference climate states. This corresponds to stronger convective updrafts in a warmer climate, which is in agreement with the stronger latent heating seen in Figure 4a,b. Above 15 km, the negative w_{cld} associated with the oscillation of a cloudy air mass around its level of neutral buoyancy due to strong overshooting convection also becomes stronger (i.e., more negative), as represented by the 1st and 10th percentiles of w_{cld}. We interpret this finding as a clear indication of a more vigorous mechanical forcing of GWs in a warming climate.

Both the in-cloud latent heating and the in-cloud vertical velocity clearly indicate that a warming climate will result in stronger tropical deep convection associated with a more vigorous generation of GWs. However, the applied analyses do not allow for an evaluation of a change in the area occupied by deep convection, and thus a change in the area in which waves are generated; that is, the amount of deep convection and GWs. Therefore, we examine profiles of the 15° S–15° N mean cloud fraction Γ_{cld}, which is shown in Figure 4e,f. Here, the lower peak in cloudiness at ~5 km can be attributed to shallow cumuli and cumuli congesti, whereas the upper peak in cloudiness at ~12.5 km can be mostly attributed to the cirrus anvils of deep convective storms. Deep convective storms themselves normally reach from the level of condensation near the top of the boundary layer (~2 km) to the upper troposphere (~10 to ~15 km). This means that all deep convective clouds must have cloudy grid cells also at the local minimum in Γ_{cld} located at an altitude of ~10 km. Thus, changes in the area covered by deep convection can be evaluated based on the absolute value of Γ_{cld} at its local minimum at ~10 km. As shown in Figure 4e,f, the absolute value of the local minimum of Γ_{cld} at ~10 km stays approximately constant in the warmer climate states. This suggests that, in contrast to its strength, the area covered by deep convection increases only little in a warmer climate, which implies that the more vigorous generation of waves should be interpreted as the generation of stronger waves (i.e., waves with a larger amplitude), instead of the more frequent generation of waves or their generation over a larger spatial area. Thus, we conclude that a warming climate will result in a strengthening of the existing tropical tropospheric wave field as a consequence of a more vigorous GW generation due to stronger deep convection.

Besides becoming stronger, Figure 4 also suggests that tropical deep convection becomes deeper in the warmer climate states by ~0.75 km for the +2 K climate states and by ~1.5 km for the +4 K climate states. A deepening of tropical convection has important implications for the dominant horizontal phase speed of the GW spectrum generated, which will be discussed in Section 4.3.

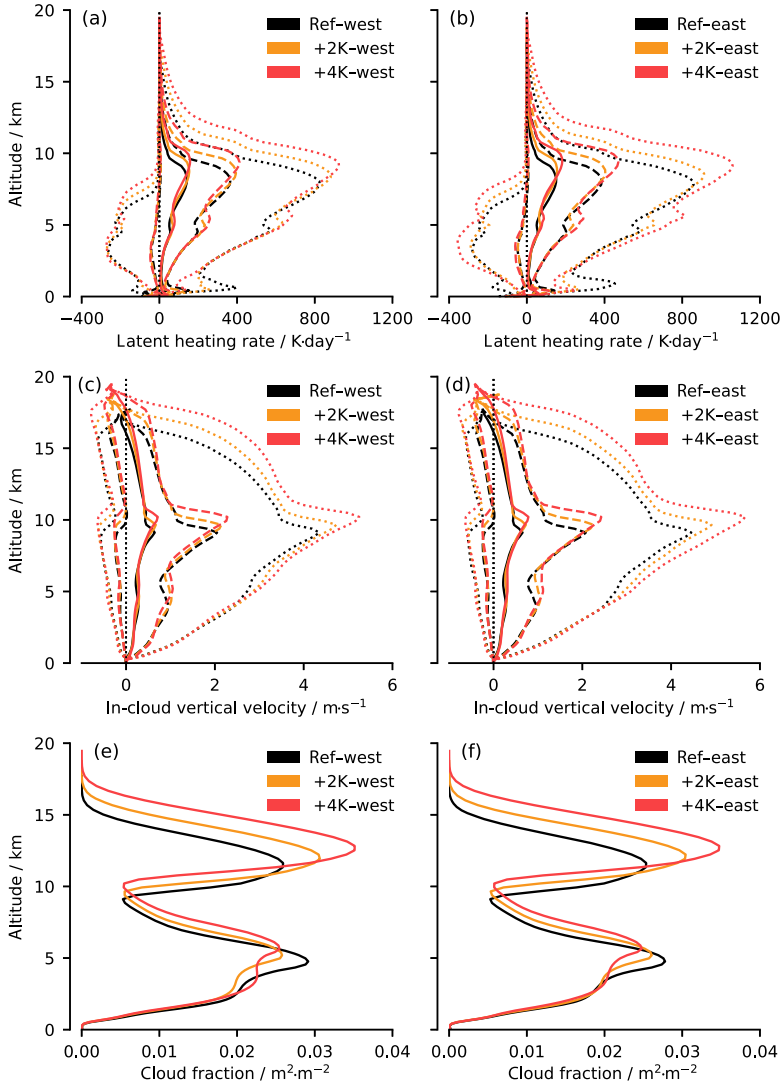

FIGURE 4 Vertical profiles of different statistics of (a, b) in-cloud latent heating Q_{lat}, (c, d) in-cloud vertical velocity w_{cld}, and (e, f) cloud fraction Γ_{cld} averaged over the last 30 simulation days. Solid lines indicate the 15° S–15° N mean value, dashed lines indicate the 10th and the 90th percentiles within 15° S–15° N, and dotted lines indicate the 1st and the 99th percentile within 15° S–15° N. The vertical dotted lines mark (a, b) an in-cloud latent heating of $Q_{lat} = 0\,\mathrm{K{\cdot}day^{-1}}$ and (c, d) an in-cloud vertical velocity of $w_{cld} = 0\,\mathrm{m{\cdot}s^{-1}}$. Panels (a), (c), and (e) show the westerly shear experiments, and panels (b), (d), and (f) show the easterly shear experiments. [Colour figure can be viewed at wileyonlinelibrary.com]

4.2 | Zonal wave scales

In order to investigate whether the strengthening of tropical deep convection has a scale preference or instead occurs uniformly across all scales, we calculate tropical mean zonal wave number power spectra of precipitation (i.e., the spectral power of precipitation as a function of zonal wave number k), as described in Section 2.4.1. The spectra and their relative difference between the warmer climate states and the corresponding reference climate state are shown in Figure 5a,c. In the warmer climate states the spectral power of precipitation is substantially larger than in the corresponding reference climate states across all zonal wave numbers. This confirms our previous finding of more vigorous convection in a warmer climate and in agreement with Parseval's theorem; it additionally agrees with the increase in tropical precipitation variance shown in Table 2. Figure 5c shows that the warming-induced strengthening of the precipitation spectra further occurs almost uniformly across all zonal wave numbers. Accordingly, the spectral shape of the precipitation spectrum does not change in the warmer climate states (Figure 5a). This suggests that the strengthening of convection is approximately uniform across its characteristic horizontal scales, ranging from individual cells to its planetary distribution associated with the land–sea distribution. In other words, convection becomes more intense in a warmer climate, but its large-scale pattern and its characteristic scales remain the same, which is in agreement with our findings in Section 4.1. These results are qualitatively consistent for the westerly and the easterly shear experiments, but for the easterly shear experiments the individual spectra have lower absolute values than the corresponding westerly shear experiments, which is consistent with Figure 3a. The root cause for this systematic difference between both sets of experiments is unclear.

Based on the changes in the tropical precipitation spectrum, we also expect the spectrum of tropical waves generated by deep convection to strengthen approximately

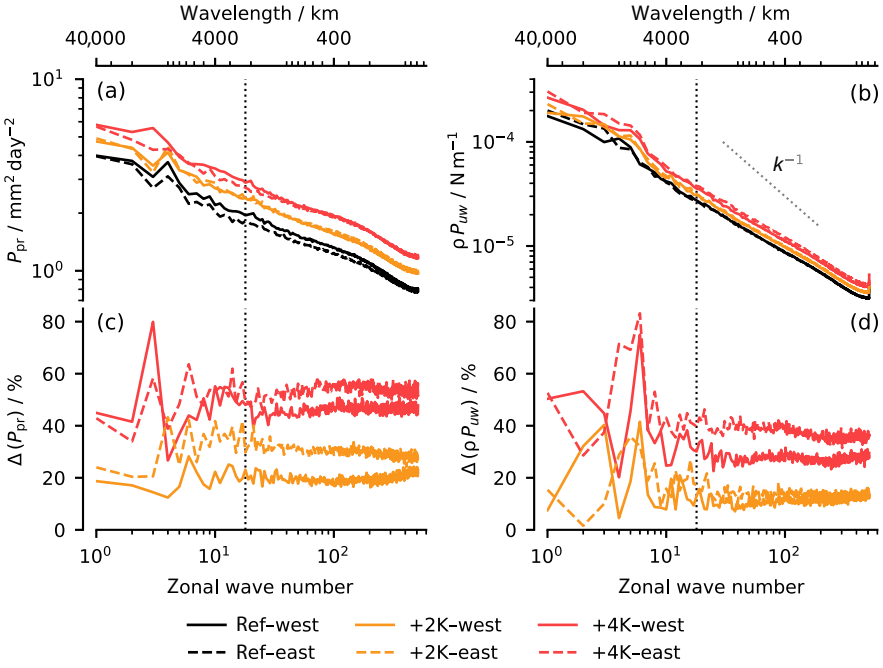

FIGURE 5 The 15° S–15° N mean (a) spectral power of precipitation P_{pr} and (b) density-weighted co-spectral power of zonal and vertical wind ρP_{uw} at an altitude of ~20 km as a function of zonal wave number k, averaged over the last 30 simulation days. The relative difference of P_{pr} and ρP_{uw} between the warmer climate states and their corresponding reference climate is shown in (c) and (d) respectively. The vertical dotted line marks $k = 18$, which is used to separate between planetary-scale waves ($k \leq 18$) and gravity waves ($k > 18$). The annotated gray dotted line in (b) highlights a spectral slope of −1. All spectra have been calculated by means of Fourier-spectral analysis (see Section 2.4.1). [Colour figure can be viewed at wileyonlinelibrary.com]

uniformly across all zonal wave numbers. This hypothesis builds on the fact that the spectra of precipitation and tropical waves are coupled in a statistical sense, even though individual convective systems of a particular horizontal scale usually generate a broad spectrum of waves; thus, features at a particular zonal wave number in the wave spectrum cannot be attributed to features at the same zonal wave number in the precipitation spectrum. Since we found the power spectrum of precipitation to increase uniformly across zonal wave number in the warmer climate states, the power spectrum of the generated waves should also increase uniformly across zonal wave number in a warmer climate, assuming that the relation between both spectra (i.e., the wave generation mechanisms) do not change in a warmer climate. To test this hypothesis, Figure 5b shows the co-spectra of zonal wind u and vertical wind w multiplied by density ρ at an altitude of ~20 km. These co-spectra can be interpreted as the zonal momentum flux spectra (i.e., the spectra of the vertical flux of zonal momentum), in the equatorial lower stratosphere (see Section 2.4.1). The wave field in the equatorial lower stratosphere is still largely determined by its tropospheric convective sources, even though filtering by zonal background winds in the upper troposphere may already cause some differences between the wave spectra in the troposphere and the lower stratosphere.

The slope of the zonal momentum flux spectra is approximately constant throughout the mesoscale ($k > 18$) and slightly shallower than −1, overall corresponding to what was found by Müller *et al.* (2018) in idealized model set-ups. The slopes of the individual power spectra of u and w are also close to their mesoscale canonical values of −5/3 (Nastrom and Gage, 1985; Gardner *et al.*, 1993; Skamarock, 2004) and 0 (Terasaki *et al.*, 2009; Skamarock *et al.*, 2014; Morfa and Stephan, 2023) respectively (not shown), indicating that ICON-A generates an overall reasonable GW spectrum. At the short wavelength tail of the zonal momentum flux spectra (Figure 5b), we notice a pronounced flattening for zonal wavelengths $\lambda_x <$ 100 km. This is an imprint of the aliasing that occurs due to the remapping from the fine ICON-A source grid ($\Delta_x \approx$ 5 km) to the coarser n256 Gaussian grid ($\Delta_x \approx 40$ km), on which we calculate the spectra. Thus, the spectra should be considered reliable only for zonal wavelengths $\lambda_x >$ 100 km, which is also well above the effective resolution of ICON-A of ~12Δx (~60 km) (Stephan *et al.*, 2019a).

Figure 5d shows the relative difference between the zonal momentum flux spectra of the warmer climate states and the corresponding reference climate state. In the GW range of the spectra – that is, $k > 18$ ($\lambda_x <$ 2,200 km) – the relative increase in spectral power is approximately uniform across all zonal wave numbers. This implies that a warmer climate would result in an approximately uniform strengthening of the existing GW spectrum in the equatorial lower stratosphere that corresponds well with the uniform strengthening of the power spectrum of precipitation (see Figure 5c). Therefore, we conclude that the generation of stronger GWs in the troposphere also results in stronger GWs in the lower stratosphere, accompanied by a net increase in GWMF entering the stratosphere. This finding may be further extendable to planetary-scale waves – that is, $k \leq 18$ ($\lambda_x \geq$ 2,200 km); however, owing to

the short analysis time span, the signal is too noisy for that claim to be certain.

The lower stratospheric zonal momentum flux spectra also show a larger warming-induced increase in spectral power for the easterly than for the westerly shear experiments for a warming of +4 K, which is in agreement with the precipitation spectra. Though the root cause for this systematic difference between both sets of experiments is unclear in the case of the precipitation spectra, in the case of the lower stratospheric zonal momentum flux spectra it could be at least partly attributable to warming-induced differences in upper tropospheric wave filtering. Warming-induced changes in upper tropospheric wave-filtering will be investigated in more detail in Section 4.3.

4.3 | Lower stratospheric GWMF

In this section we analyze changes in GWMF at an altitude of ~20 km to investigate how the momentum carried by GWs (which is potentially available for driving the QBO) may change in a warmer climate. In order to quantify the GWMF we applied the S3D method because of the limitations of classical Fourier spectral methods (see Section 2.4.2).

Figure 6 shows that the warming-induced strengthening of the GW field in the equatorial lower stratosphere – indicated by the changes in the power spectra (Figure 5b) – results in a clear increase of the zonal GWMF at an altitude of ~20 km. For both sets of experiments, both the eastward GWMF and the westward GWMF are stronger in the warmer climate states than in the reference climate, and this strengthening is larger in the +4 K-climate states than in the +2 K-climate states. For the westerly shear experiments, the increase in eastward GWMF and westward GWMF seems to scale approximately linearly with the amount of warming, whereas this is clearly not the case for the easterly shear experiments. Here, the eastward GWMF increases much more strongly for the +4 K-climate state compared with the +2 K-climate state, whereas the increase of the westward GWMF is approximately the same for the +4 K-climate state and the +2 K-climate state.

In order to be available for the acceleration of the QBO jets, the warming-induced increase in GWMF must be carried by waves with zonal phase speeds relevant for the QBO. Thus, we have a look at the distribution of GWs as a function of their ground-based zonal phase speed c_x, which is determined by the S3D method (see Section 2.4.2). Given there are, in total, N valid GW samples detected by the S3D method, each of them associated with a zonal GWMF B_x and a ground-based zonal phase speed c_x, we

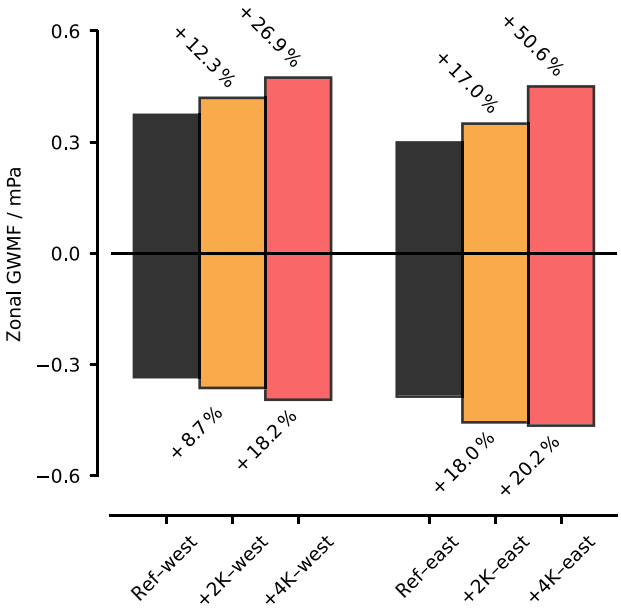

FIGURE 6 Zonal mean zonal gravity wave momentum flux (GWMF; i.e., vertical flux of zonal wave momentum) at an altitude of 20 km averaged over 15° S–15° N for the last 30 simulation days. Positive bars show eastward GWMF and negative bars show westward GWMF. Annotations show the increase in eastward and westward GWMF of the warmer climate states relative to their corresponding reference climate. The zonal GWMF has been calculated by means of the small-volume few-wave decomposition (S3D; see Section 2.4.2). [Colour figure can be viewed at wileyonlinelibrary.com]

get the normalized zonal GWMF distribution as a function of zonal phase speed as $B_x(c_x)/N$ (Figure 7a,b). $B_x(c_x)/N$ is commonly referred to as the zonal GWMF spectrum and can be further separated into

$$\frac{B_x(c_x)}{N} = \frac{n(c_x)}{N}\frac{B_x(c_x)}{n(c_x)}, \tag{5}$$

where $n(c_x)$ is the absolute GW frequency distribution as a function of ground-based zonal phase speed. Accordingly, the first term on the right-hand side of Equation 5, $n(c_x)/N$, denotes the relative GW frequency distribution as a function of ground-based zonal phase speed (Figure 7c,d), and the second term on the right-hand side of Equation 5, $B_x(c_x)/n(c_x)$, denotes the mean zonal GWMF associated with a wave for a given ground-based zonal phase speed (Figure 7e,f).

As shown by Figure 7a,b, both the eastward GWMF and the westward GWMF increase in a warmer climate nearly across the entire considered phase speed range of $-60\,\mathrm{m\cdot s^{-1}} \le c_x \le +60\,\mathrm{m\cdot s^{-1}}$. This holds true for both sets of experiments. The majority of the GWMF increase is associated with waves that have a zonal phase speed relevant for the QBO ($-40\,\mathrm{m\cdot s^{-1}} \lesssim c_x \lesssim +20\,\mathrm{m\cdot s^{-1}}$; see Figure 1; please note that the relevant phase speed

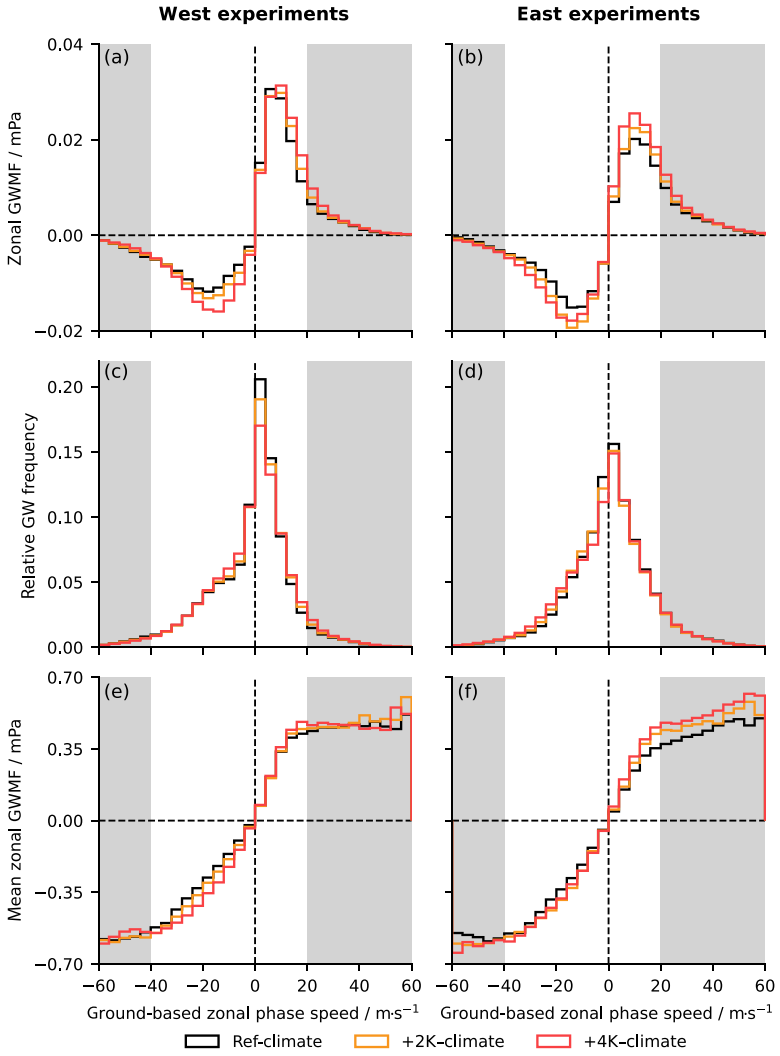

FIGURE 7 Different gravity wave (GW) distributions as a function of ground-based zonal phase speed within 15° S–15° N at an altitude of 20 km, averaged over the last 30 simulation days: (a, b) distribution of zonal gravity wave momentum flux (GWMF), (c, d) relative frequency distribution of GWs, and (e, f) distribution of mean zonal GWMF per phase speed bin. Panels (a), (c), and (e) show the westerly shear experiments and panels (b), (d), and (f) show the easterly shear experiments. Light gray shading highlights zonal phase speeds, which exceed the fastest 5° S–5° N mean zonal winds between an altitude of 15 and 40 km and during the last 30 simulation days. Thus, GWs with these zonal phase speeds likely do not contribute in driving the quasi-biennial oscillation. The zonal GWMF and the ground-based zonal phase speed have been calculated by means of the small-volume few-wave decomposition (see Section 2.4.2). [Colour figure can be viewed at wileyonlinelibrary.com]

range itself may also differ slightly between the different climate states). Only the small fraction of the GWMF increase that is associated with waves with $+20\,\mathrm{m}\cdot\mathrm{s}^{-1} \leq c_x \leq +30\,\mathrm{m}\cdot\mathrm{s}^{-1}$ is not relevant for the QBO. Thus, we expect the strengthening of the lower stratospheric GW field to ultimately have a significant impact onto the QBO. This finding is in contrast to Kawatani *et al.* (2011), who found that the total zonal wave momentum flux predominantly increases at zonal phase speeds that are irrelevant for the QBO.

Figure 7c–f shows that the root cause for the increase of zonal GWMF at most zonal phase speeds relevant for the QBO is twofold. First, the zonal GWMF that is on average carried by a GW increases in the warmer climate states for most of these phase speeds (Figure 7e,f). Following Equation 3, this means that the GWs have a larger amplitude on average or, to put it simply, are stronger. This confirms our findings from Section 4.1, in which we found that a warmer climate will result in the generation of stronger convective GWs. Second, the relative frequency distribution of the GWs tends to shift towards higher phase speeds (Figure 7c,d), which are stronger on average, independent of the climate state (Figure 7e,f). For both sets of experiments, the relative frequency of slow GWs with zonal phase speeds close to $0\,\mathrm{m}\cdot\mathrm{s}^{-1}$ decreases and the relative frequency of faster waves increases in the warmer climate states, especially for GWs propagating eastward (westward) in the westerly (easterly) shear experiments. Furthermore, this shift towards faster zonal phase speeds is more pronounced in the +4 K climate states than in the +2 K climate states, suggesting a physical root cause for this behavior.

We propose that the shift towards faster zonal phase speeds is a consequence of the warming-induced deepening of the convective latent heating. As shown in Figure 4a,b, the imposed warming not only causes an increase in the overall and peak latent heating but also an increase in its vertical depth, which is in agreement with the deepening of the troposphere found in Section 3.1. Salby and Garcia (1987) showed that a purely thermally forced wave has a preferred vertical wavelength of twice the vertical scale of the latent heating profile. Thus, we

expect the increase of the latent heating depth d_{LH} in a warmer climate to result in an increase of the average vertical wavelength λ_z of the GWs. However, the vertical wavelength itself is coupled to its intrinsic horizontal phase speed $c_h - \overline{u}_h$, as shown by the simplified dispersion relation of medium-frequency GWs (compare Eq. 33 of Fritts and Alexander, 2003):

$$|c_h - \overline{u}_h| = \frac{N|\lambda_z|}{2\pi}, \tag{6}$$

where N is the buoyancy frequency, $\overline{u}_h$ is the local horizontal background wind, and c_h is the GW's horizontal ground-based phase speed. Thus, the warming-induced deepening of the latent heating would ultimately cause an increase in the ground-based horizontal phase speed of thermally forced GWs. Assuming that N and $\overline{u}_h$ in the tropical troposphere stay constant at their average values of $N = 0.0075\,s^{-1}$ and $\overline{u}_h = 0\,m{\cdot}s^{-1}$ independent of the climate state, which is reasonable to a first approximation, the observed deepening of the mean latent heating depth d_{LH} by ~0.75 km (~1.5 km) for the +2 K (+4 K) climate states (see Figure 4a,b) would result in an increase of the ground-based horizontal phase speed c_h by ~1.8 $m{\cdot}s^{-1}$ (~3.6 $m{\cdot}s^{-1}$), assuming $2d_{LH} = \lambda_z$. Assuming that the GWs have no preferred horizontal propagation direction, the average horizontal and zonal phase speed relate as $|c_h| = |\sqrt{2}c_x|$. Thus, based on the observed increase of d_{LH}, we would ultimately expect an increase of the tropospheric $|c_x|$ by ~1.3 $m{\cdot}s^{-1}$ and ~2.5 $m{\cdot}s^{-1}$ for the +2 K climate states and the +4 K climate states respectively. Our S3D results show an increase of $|c_x|$ in the lower stratosphere by ~0.38 $m{\cdot}s^{-1}$ and ~0.91 $m{\cdot}s^{-1}$. Given the assumptions made in our idealized calculation, the warming-induced changes in latent heating depth d_{LH} and ground-based zonal phase speed c_x agree surprisingly well. Thus, we conclude that the observed shift towards faster zonal phase speeds can be reasonably attributed to the warming-induced deepening of the latent heating profile.

Coming back to the GWMF in the lower stratosphere, we further investigated the role of potential warming-induced changes in upper tropospheric wave filtering. Based on the warming-induced westerly anomaly of the zonal wind in the upper equatorial troposphere for both sets of experiments (see Figure 2d), one would expect that slow eastward-propagating waves are increasingly filtered out in the warmer climate states, whereas slow westward-propagating waves can propagate vertically increasingly well. However, only for the westerly shear experiments do we notice that the zonal GWMF associated with slow eastward-propagating GW with $c_x \leq 8\,m{\cdot}s^{-1}$ decreases in the warmer climate states and the zonal GWMF associated with slow westward-propagating GWs $c_x \geq -12\,m{\cdot}s^{-1}$ strongly increases (Figure 5a). For the easterly shear experiments, we do not find similar warming-induced changes in upper tropospheric filtering of slow eastward-propagating waves at all. Therefore, we conclude that the impact of warming-induced changes in upper tropospheric wave filtering is overall minor compared with the general warming-induced increase of lower stratospheric GWMF due to stronger convection. At least partly, this may also be a consequence of the observed increase in the mean zonal phase speed of the GWs, which makes it potentially less likely for a wave to reach a critical level. Nevertheless, methodological uncertainties of the S3D method and the local nature of small-scale GW filtering, which may not be captured by zonal mean views, may also explain why we only see very small changes in upper tropospheric wave filtering.

5 | CHANGES IN THE QBO

5.1 | General aspects of the explicitly simulated QBO in ICON-A

As shown by Giorgetta *et al.* (2022), the global storm-resolving set-up of ICON-A used in our study simulates a downward propagation of the QBO jets as a product of resolved wave–mean flow interactions and advection by the tropical upwelling throughout a period of 45 days. However, the downward propagation of the QBO jets in ICON-A is much too fast compared with ERA5 above 27 km, which Giorgetta *et al.* (2022) attribute to a too strong total wave forcing. This finding corresponds to the fact that current GSRMs with high horizontal resolutions of $\Delta x < 10$ km tend to have difficulties in simulating the total resolved wave momentum fluxes and the resulting wave forcing accurately (Stephan *et al.*, 2019a; Stephan *et al.*, 2019b; Polichtchouk *et al.*, 2021). In our experiments, the too fast QBO is illustrated by the descent rates of the upper QBO shear zone between 30 and 40 km, which in our reference experiments has an average value of ~130 $m{\cdot}day^{-1}$ and ~100 $m{\cdot}day^{-1}$ during the last 30 simulation days for the easterly and westerly shear experiments, respectively (see Figure 8a,d). Giorgetta *et al.* (2022) further showed that the magnitude of the QBO jets was sustained realistically throughout their simulation. This also applies to all simulations of this study, as shown by Figure 8.

In the lower stratosphere, ICON-A also reveals some of the common QBO biases of GCMs – (see Anstey *et al.*, 2022, for an overview): namely, a lack of downward propagation and a too weak amplitude. Giorgetta *et al.* (2022) showed that ICON-A does not simulate a reasonable downward propagation of the QBO jets below 25 km down to the

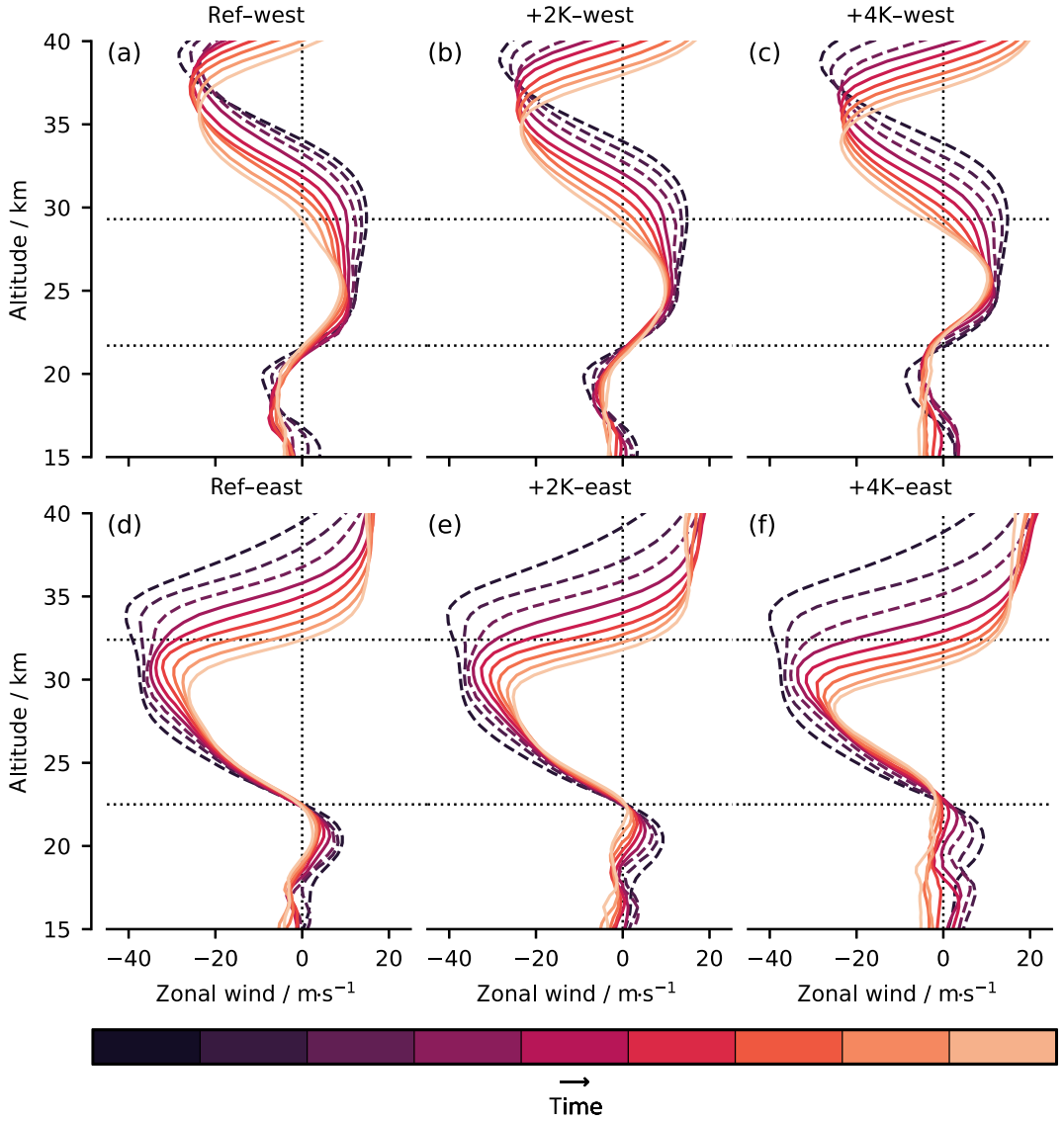

FIGURE 8 Five-day mean 5° S–5° N zonal mean zonal wind profiles throughout (a) the experiments initialized with the quasi-biennial oscillation (QBO) in its westerly phase and (b) the experiments initialized with the QBO in its easterly phase. The colours indicate the different five-day periods, thereby highlighting the downward propagation of the QBO throughout each experiment. The first three five-day periods, which are within the spin-up period, are marked by dashed lines. Horizontal dotted lines are plotted for highlighting differences between the experiments. [Colour figure can be viewed at wileyonlinelibrary.com]

tropopause, which is also clearly demonstrated by the stalling of the lowermost QBO shear zone below 25 km in our reference experiments (Figure 8a,d). Furthermore, for the easterly shear experiment, the lowermost QBO jet is too weak compared with ERA5 (not shown). Insufficient vertical resolution is commonly believed to be one potential root cause for the weak amplitude bias in the lowermost stratosphere (Anstey *et al.*, 2022, and references therein), and using a high vertical resolution of $\Delta z \lesssim$ 500 m has been shown to reduce this bias significantly (Garcia and Richter, 2019). Given the high vertical resolution of $\Delta z \approx 375$ m in the lower stratosphere in our ICON-A set-up, the weak amplitude bias of the simulated QBO in the lowermost stratosphere is thus at least surprising and is planned to be addressed in a future study.

Since the general deficiencies of the simulated QBO in ICON-A are shared throughout all experiments, we do not expect them to have a significant influence on the comparison between the different climate states. Nevertheless, they should be borne in mind for further interpretation of our results.

5.2 | Downward propagation of QBO shear zones

Figure 8 shows the temporal evolution of the QBO jets throughout the experiments and allows for a direct evaluation of how the downward propagation of the QBO jets changes in the warmer climate states. The upper shear zone, initially located around or above ~35 km, propagates downward at an increasingly faster rate in the warmer climate states. Consequently, with respect to the reference climate, the zero-wind line of the upper shear zone at the end of the experiments is located ~1 km lower in the +2 K climates and ~1 km (westerly shear experiment) or ~2 km (easterly shear experiment) lower in the +4 K climates, where we attribute the difference in the case of the +4 K climates to internal variability. Based on the faster downward propagation of the upper QBO shear zones, we would ultimately expect the QBO to speed up in a warmer climate; that is, to have a shorter period. However, it should be noted that a substantial part of the speed-up of the downward propagation of the upper shear zone occurs during the initial 15 days of the simulations and, therefore, is likely influenced by the model spin-up. In contrast to the upper shear zone, the lower shear zone of the QBO (between 22 and 25 km in the westerly shear experiments, between 22 and 28 km in the easterly shear experiments) is increasingly shifted upward with time in the warmer climate states compared with the reference climate, especially for the +4 K climates. Differences between the easterly and westerly shear experiments are negligible. Owing to the short simulation period, we were not able to identify the root cause for this upward shift of the lower QBO shear zone.

In order to investigate the forcing of the faster downward propagation of the upper QBO shear zone, we created so-called QBO composite profiles. In our case, these QBO composite profiles refer to those 11-day mean zonal wind profiles for which the $-10\,\mathrm{m\cdot s^{-1}}$-wind line is closest to an altitude of 32 km. These profiles are shown in Figure 9a. We chose an averaging period of 11 days as a pragmatic compromise between a robust, comparable mean and the unintended smoothing of potential warming signals. We chose the specific reference point based on the rather pragmatic consideration that it is one of the only possible reference points that lie within the upper QBO shear zone during the last 30 days of each set of experiments. This method allows a comparison of the QBO forcing between the different experiments at a fixed height instead of at a fixed time, which is necessary due the different downward propagation rates of the QBO shear zones in the different experiments. Figure 9b shows the total zonal wind tendency during the 11-day period of each composite. The strongest total tendencies are located in the upper QBO shear zone, indicating its wave-driven downward propagation. Apart from experiment +2 K-east, the total tendencies in the warmer climate states become larger, indicating a stronger downward forcing of the QBO jets, which agrees with the faster downward propagation of the shear zones seen in Figure 8. For experiment +2 K-east, we attribute the lack of increase in total tendency to internal variability, which may still be considerable during only 11 days of analysis.

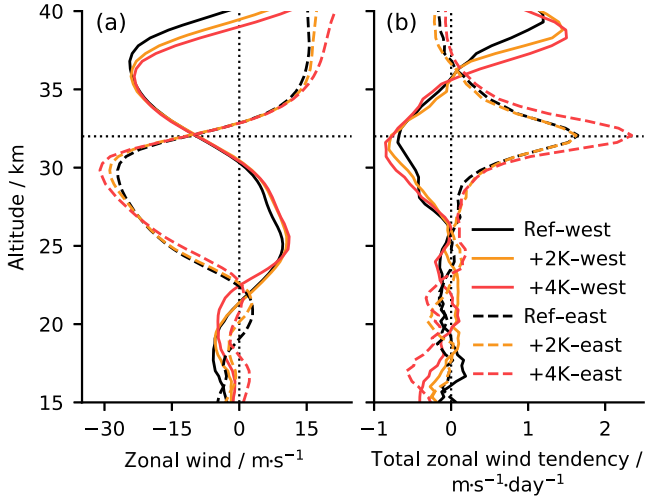

FIGURE 9 The 5° S–5° N mean QBO composites of the 11-day period during which the zonal mean zonal wind profiles cross the $-10\,\mathrm{m\cdot s^{-1}}$-wind line closest at a reference height of 32 km: (a) zonal wind and (b) total zonal wind tendency. The reference height is marked by the horizontal dotted black line. [Colour figure can be viewed at wileyonlinelibrary.com]

5.3 | Magnitude of QBO jets

In order to assess warming-induced anomalies in the magnitude of the QBO jets, we compare the composites of the QBO zonal wind profiles shown in Figure 9a. These composite profiles show three distinct QBO jets in the stratosphere: a weak jet in the lowermost stratosphere centered around ~20 km, the core QBO jet centered at ~25 km and ~30 km for the westerly and easterly shear experiments respectively, and the uppermost QBO jet centered slightly above 35 km. The lowermost QBO jet centered around ~20 km weakens in the warmer climate states for both sets of experiments, but the weakening appears to be slightly stronger for the easterly shear experiments. It should be noted, however, that this result is probably strongly influenced by the rapid general erosion of the lower jet associated with the strong weak amplitude bias of the simulated QBO in ICON-A (see Section 5.1), even though a decrease in the magnitude of the

lowermost QBO jet is in agreement with previous studies that identified a decrease in QBO amplitude in the lowermost stratosphere due to a speed-up of the tropical upwelling associated with the BDC (Kawatani *et al.*, 2011; Kawatani and Hamilton, 2013; Richter *et al.*, 2020).

The peak magnitude of the core QBO jet, which is centered at 30 km for the easterly shear experiments and at 25 km for the westerly shear experiments, increases for both sets of experiments. The relative increase is very similar between both sets of experiments despite the different absolute strength of the jet. For the easterly shear experiments, the peak magnitude increases by 6.4% for the +2 K-climate and by 14.5% for the +4 K-climate. For the westerly shear experiments, the peak magnitude increases by 9.4% for the +2 K-climate and by 15.1% for the +4 K-climate. This strengthening of the core QBO jets in both sets of experiments would correspond to an increase in QBO amplitude in the central stratosphere between ~24 and ~32 km. We suggest that the root cause for the strengthening of the core QBO jet is the warming-induced increase in the mean zonal phase speed of the GWs due to a deepening of the convective latent heating (see Section 4.3). As shown by Saravanan (1990) and Geller *et al.* (2016b), the QBO amplitude depends mainly on the magnitude of the phase speeds of the waves that drive the QBO. Both studies found that the QBO jets are stronger if the mean absolute phase speed of the waves is larger, and vice versa. Thus, an increase of the upper QBO amplitude is reasonable based on the observed shift of the GW spectrum towards faster zonal phase speeds. However, this result strongly disagrees with previous model studies using coarse-resolution GCMs with GW parametrization. These models typically project a decrease of the QBO amplitude in a warmer climate basically throughout the whole QBO vertical domain (Kawatani *et al.*, 2011; Kawatani and Hamilton, 2013; Richter *et al.*, 2020), despite some of them using interactive GW parametrizations that are coupled to convection and which should in principle, therefore, be able to reproduce this mechanism discussed here.

For the uppermost QBO jet, which is centered slightly above 35 km, the warming-induced zonal wind anomaly differs between both sets of experiments. The jet magnitude increases for the easterly shear experiments, whereas it decreases for the westerly shear experiments. We suggest that this difference is caused by the different sign of the vertical advection associated with the secondary meridional circulation of the QBO jets, which dominates the vertical movement in this altitude range (not shown). In addition, in the case of the easterly experiments, which are initialized on April 1, 2005, the uppermost westerly jet is a jet of the semiannual oscillation rather than of the QBO (see Fig. 1 of Pahlavan *et al.*, 2021), and thus changes in semiannual oscillation dynamics may also be causal for the strengthening of the jet in the warmer climate states.

6 | SUMMARY, DISCUSSION, AND CONCLUSIONS

In this study, we performed global storm-resolving simulations of three idealized climate states to investigate how tropical GWs and the QBO may change in a warming climate. For the simulations, we used the GSRM ICON-A, which explicitly resolves deep convection and GWs and thus does not employ corresponding parametrizations. In the warmer climate states, we found stronger convectively generated GWs across all scales due to a strengthening of tropical deep convection. As a consequence, the GWMF in the lower stratosphere at zonal phase speeds relevant for the QBO increases substantially, especially for westward-propagating GWs, due to changes in upper tropospheric wave filtering. The QBO itself speeds up in the warmer climate states but, at the same time, shows an increasingly strong weak amplitude bias in the lowermost stratosphere. Additionally, we found that in the warmer climate states the QBO jets in the lower stratospherr weaken while the QBO jets in the upper stratosphere strengthen. We attribute the strengthening of the upper stratospheric QBO jets to a shift of the GW spectrum towards faster phase speeds, which itself is caused by a deepening of the convective latent heating profile.

The substantial increase of the total lower stratospheric GWMF in the warmer climate states agrees well with the results of those QBOi models that use an interactive GW parametrization coupled to convective heating based on Beres *et al.* (2004) (see Richter *et al.*, 2020). Thus, the Beres *et al.* (2004) parametrization is apparently the only GW parametrization in the QBOi model ensemble that can adequately capture the substantial changes in convective GW generation which we found in the warmer climate states. The agreement between our results and the Beres *et al.* (2004) parametrization is not surprising given that it is the most physics-based parametrization in the QBOi model ensemble and the only one with a variable GW source level. In contrast, even slightly less sophisticated interactive GW parametrizations with a fixed GW source level are not capable of capturing the increase of the GWMF in the lower stratosphere found in our explicit simulations. The same holds true for parametrizations using a fixed GW source spectrum and source level (see Richter *et al.*, 2020). Thus, our results clearly indicate that an advanced physics-based GW parametrization in conventional GCMs is necessary for being able to model a realistic response of the GWMF to a warming climate.

Our results further show that the impact of changes in upper tropospheric wave-filtering on the total GWMF in the lower stratosphere is clearly minor compared with the overall increase in tropospheric wave sources. This is in agreement with the results of Richter *et al.* (2020), who also found no significant changes in upper tropospheric wave-filtering in the QBOi models. Therefore, we conclude that a decrease of the GWMF in the lower stratosphere in the Tropics in a warming climate can be virtually ruled out and a robust increase seems to be increasingly likely, with corresponding implications for the QBO.

However, it should be recognized that the horizontal resolution of ∼5 km in our simulations is likely still too coarse to resolve the short wavelength tail of the GW spectrum sufficiently, as shown by Lane and Knievel (2005) and Polichtchouk *et al.* (2021). Following Lane and Knievel (2005) and Polichtchouk *et al.* (2021), we therefore think that the GWMF at long and mesoscale wavelengths with 2,200 km $< \lambda_h <$ 100 km is artificially enhanced in our simulations due to an overestimation of the dominant horizontal wavelength. Whether this enhancement leads to an overestimation of the total GWMF in our simulations remains unclear. Though Polichtchouk *et al.* (2021) found that the horizontal resolution only impacts the partitioning of GWMF across wavelengths but not the total GWMF, Lane and Knievel (2005) found that the overestimation of the dominant wavelength may reduce trapping and filtering of GWs and thus can also result in an overestimation of the total GWMF. However, given that all simulations were run with the same model set-up and that warming-induced anomalies in the zonal wave number spectra are approximately uniform across all scales (see Figure 5), we expect the impact of potential GWMF overestimations on the previously drawn conclusions to be minor.

As a consequence of the increased GWMF in the lower stratosphere, we found the downward propagation of the QBO to accelerate in the warmer climate states. This would ultimately correspond to a shortening of the QBO period in a warming climate, but it must be mentioned that this conclusion should be considered tentative due to the very short simulation period of our experiments. A shortening of the QBO period, in turn, would agree with those QBOi models that employ the advanced Beres *et al.* (2004) GW parametrization. Based on these results, and given that those QBOi models showing a lengthening of the QBO period employ rather primitive GW parametrizations (see Richter *et al.*, 2020), there appears to be some indication that a substantial lengthening of the QBO period in a warming climate may be rather unlikely.

However, the quantitative extent of any potential change in the QBO period will probably remain very model dependent, and thus highly uncertain, even for those GCMs employing advanced physics-based GW parametrizations or simulating GWs explicitly. This is due to the large intermodel variability in the other QBO forcing terms; that is, vertical advection by tropical upwelling and resolved planetary-wave forcing. Richter *et al.* (2020) showed that even though the qualitative response of these two QBO forcing terms to a warming climate is certain, large quantitative differences in the response remain. Additional uncertainty in changes of the QBO wave forcing stems from its strong dependency on the waves' phase speeds at which the changes occur. For example, the warming-induced increase of GWMF in our simulations occurs nearly entirely at phase speeds relevant for the QBO, whereas the increase of the resolved wave momentum flux in the simulations of Kawatani *et al.* (2011) occurs nearly entirely at phase speeds not relevant for the QBO. We think that this spectral uncertainty in the QBO wave forcing could be in part related to the parametrization of deep convection in coarse-resolution GCMs. Therefore, additional simulations of the QBO with different GSRMs, which represent deep convection and GWs explicitly, are desirable to further constrain the response of the QBO to a warming climate quantitatively. However, even for GSRMs, the parametrization of remaining unresolved dynamics, such as vertical diffusion, and the choice of the dynamical core itself will potentially cause intermodel spread (Yao and Jablonowski, 2015). Stephan et al. (2019b) further showed that in GSRMs there is also still a substantial intermodel spread in simulated GWMF.

Nevertheless, a first quantitatively more constrained estimate of changes in the QBO downward propagation rate for a single GSRM is urgently needed as a future baseline, but this cannot be provided by the short simulations of this study. The main reason for this is internal climate variability, which likely is considerable in our simulations, at least for the large-scale, low-frequency QBO forcing by planetary waves and residual advection associated with tropical upwelling. Additionally, any warming-induced change in the QBO momentum budget is likely specific to our selected simulation period of boreal spring, as both tropical wave activity associated with the latitudinal movement of the ITCZ (e.g., Vincent and Alexander, 2000) and tropical upwelling (e.g., Abalos *et al.*, 2012) exhibit a substantial seasonal cycle. Therefore, our estimates of changes in the rate of QBO downward propagation may not be extendable to longer time-scales. Consequently, simulations of at least one whole QBO cycle for a current reference climate state and a future warmer climate state are clearly necessary to determine a quantitatively more robust estimate of warming-induced changes in the QBO momentum balance in ICON-A, and these are planned for

future research. To determine a robust change in the QBO period itself, even longer simulations of several QBO cycles would be necessary, which is currently not feasible due to computational constraints.

An interesting finding in our simulations is the warming-induced strengthening of the QBO jets in the middle stratosphere around an altitude of ∼30 km independent of QBO phase, which would correspond to an increase in QBO amplitude. The simulated warming-induced shift of the GW spectrum towards faster zonal phase speeds gives a plausible explanation for this finding based on the established link between the width of the zonal phase speed spectrum of the waves and the QBO amplitude (Saravanan, 1990; Geller *et al.*, 2016b). Also, observational data from the last ∼70 years, during which a warming of ∼1 K has already taken place (NOAA, 2022), show an increase in QBO amplitude between 30 hPa and 10 hPa (∼25 to 32 km) (Kawatani and Hamilton, 2013; Anstey *et al.*, 2022). However, in contrast to our results and the observational record, conventional GCMs usually simulate a warming-induced decrease in QBO amplitude throughout the whole vertical QBO domain (see e.g. Anstey *et al.*, 2022, and references therein). Though the reasons for the disagreement between the observations and the conventional GCMs have been unclear so far, our results appear to give some new indication that model deficiencies of the conventional GCMs might be a potential root cause. However, here also, longer simulations are essential to support this suggestion, and the uncertainties in simulated GW spectra in current GSRMs with high horizontal resolutions of $\Delta x < 10$ km (Stephan *et al.*, 2019a; Stephan *et al.*, 2019b; Polichtchouk *et al.*, 2021) should be considered when interpreting changes in GW phase speeds.

In conclusion, we think that our study has shifted the uncertainty in QBO projections. Based on our results, it is now no longer unclear whether the GW forcing of the QBO will increase or decrease in a warming climate but instead whether the strengthening of the tropical upwelling or the strengthening in the total wave forcing will have a larger effect on the QBO in a warming climate. Depending on which factor will outweigh the other, the QBO will either accelerate or decelerate. This shift in uncertainty achieved by our study is already a major step forward, as it allows us to reject models employing unreliable GW parametrizations from the ensemble of potential QBO responses to a warming climate. However, we expect the net effect of the increase in the different QBO forcing terms to remain substantially model dependent, at least quantitatively. For now, we thus expect QBO projections to remain overall uncertain.

AUTHOR CONTRIBUTIONS

Henning Franke: conceptualization; data curation; formal analysis; investigation; methodology; software; visualization; writing – original draft; writing – review and editing. **Peter Preusse:** investigation; methodology; software. **Marco Giorgetta:** conceptualization; funding acquisition; investigation; methodology; project administration; resources; supervision.

ACKNOWLEDGEMENTS

We thank the German Federal Ministry of Education and Research (BMBF) for partial support through the program Role of the Middle Atmosphere in Climate (ROMIC II: QUBICC) and PRACE for awarding us access to Piz Daint at the Swiss National Supercomputing Centre (CSCS) and JUWELS Booster at the Forschungszentrum Jülich (allocation no. 2019215178). The analysis of the experiments has been done on the supercomputers Mistral and Levante of the German Climate Computing Center DKRZ. We further acknowledge the Integrated Climate Data Center (ICDC), the Center for Earth System Research and Sustainability (CEN), and the University of Hamburg for supporting the IMERG data. In addition, we want to express our gratitude to Andrea Schneidereit, Dina Khordakova, Manfred Ern, Young-Ha Kim, and Ulrich Achatz for many valuable discussions and helpful comments during the early stages of the manuscript. We thank Claudia Stephan for an internal review of the initial manuscript at the Max Planck Institute for Meteorology, Ed Gerber for editing, and two anonymous reviewers for their comments and suggestions that greatly improved the final version of the manuscript. Open Access funding enabled and organized by Projekt DEAL.

CONFLICT OF INTEREST STATEMENT

The authors declare that they have no conflict of interest.

DATA AVAILABILITY STATEMENT

The ICON-A source code and scripts that are necessary to reproduce the model simulations of this study and all the analysis code that is necessary to reproduce the results of this study, except for the S3D source code and S3D analysis scripts, are available at https://www.wdc-climate.de/ui/entry?acronym=DKRZ_LTA_081_ds00002 (Franke *et al.*, 2023). The release versions of the ICON-A source code are available to individuals under license as described by MPI-M (2023). By downloading the ICON-A source code, the user accepts the license agreement. S3D source code can be obtained by contacting Peter Preusse; S3D analysis scripts can be obtained by contacting Henning Franke.

ORCID

Henning Franke https://orcid.org/0000-0001-9527-2946
Marco Giorgetta https://orcid.org/0000-0002-4278-1963

REFERENCES

Abalos, M., Randel, W.J. and Serrano, E. (2012) Variability in upwelling across the tropical tropopause and correlations with tracers in the lower stratosphere. *Atmospheric Chemistry and Physics*, 12, 11505–11517.

Anstey, J.A., Banyard, T.P., Butchart, N., Coy, L., Newman, P.A., Osprey, S. and Wright, C.J. (2021) Prospect of increased disruption to the QBO in a changing climate. *Geophysical Research Letters*, 48, e2021GL093058.

Anstey, J.A., Osprey, S.M., Alexander, J., Baldwin, M.P., Butchart, N., Gray, L., Kawatani, Y., Newman, P.A. and Richter, J.H. (2022) Impacts, processes and projections of the quasi-biennial oscillation. *Nature Reviews Earth & Environment*, 3, 588–603.

Anstey, J.A. and Shepherd, T.G. (2014) High-latitude influence of the quasi-biennial oscillation. *Quarterly Journal of the Royal Meteorological Society*, 140, 1–21.

Baldwin, M.P., Gray, L.J., Dunkerton, T.J., Hamilton, K., Haynes, P.H., Randel, W.J., Holton, J.R., Alexander, M.J., Hirota, I., Horinouchi, T., Jones, D.B.A., Kinnersley, J.S., Marquardt, C., Sato, K. and Takahashi, M. (2001) The quasi-biennial oscillation. *Reviews of Geophysics*, 39, 179–229.

Beres, J.H., Alexander, M.J. and Holton, J.R. (2004) A method of specifying the gravity wave spectrum above convection based on latent heating properties and background wind. *Journal of the Atmospheric Sciences*, 61, 324–337.

Butchart, N., Anstey, J.A., Hamilton, K., Osprey, S., McLandress, C., Bushell, A.C., Kawatani, Y., Kim, Y.-H., Lott, F., Scinocca, J., Stockdale, T.N., Andrews, M., Bellprat, O., Braesicke, P., Cagnazzo, C., Chen, C.-C., Chun, H.-Y., Dobrynin, M., Garcia, R.R., Garcia-Serrano, J., Gray, L.J., Holt, L., Kerzenmacher, T., Naoe, H., Pohlmann, H., Richter, J.H., Scaife, A.A., Schenzinger, V., Serva, F., Versick, S., Watanabe, S., Yoshida, K. and Yukimoto, S. (2018) Overview of experiment design and comparison of models participating in phase 1 of the SPARC quasi-biennial oscillation initiative (QBOi). *Geoscientific Model Development*, 11, 1009–1032.

Butchart, N., Anstey, J.A., Kawatani, Y., Osprey, S.M., Richter, J.H. and Wu, T. (2020) QBO changes in CMIP6 climate projections. *Geophysical Research Letters*, 47, e2019GL086903.

Butchart, N., Scaife, A.A., Bourqui, M., de Grandpré, J., Hare, S.H.E., Kettleborough, J., Langematz, U., Manzini, E., Sassi, F., Shibata, K., Shindell, D. and Sigmond, M. (2006) Simulations of anthropogenic change in the strength of the brewer–Dobson circulation. *Climate Dynamics*, 27, 727–741.

Collimore, C.C., Martin, D.W., Hitchman, M.H., Huesmann, A. and Waliser, D.E. (2003) On the relationship between the QBO and tropical deep convection. *Journal of Climate*, 16, 2552–2568.

Coy, L., Newman, P.A., Pawson, S. and Lait, L.R. (2017) Dynamics of the disrupted 2015/16 quasi-biennial oscillation. *Journal of Climate*, 30, 5661–5674.

Deser, C., Tomas, R.A. and Sun, L. (2015) The role of ocean-atmosphere coupling in the zonal-mean atmospheric response to arctic sea ice loss. *Journal of Climate*, 28, 2168–2186.

Durack, P.J. and Taylor, K.E. (2019) PCMDI AMIP SST and sea-ice boundary conditions version 1.1.6.

Ern, M., Hoffmann, L. and Preusse, P. (2017) Supporting information for "directional gravity wave momentum fluxes in the stratosphere derived from high-resolution AIRS temperature data". *Geophysical Research Letters*, 44, 1–22.

Ern, M., Preusse, P., Alexander, M.J. and Warner, C.D. (2004) Absolute values of gravity wave momentum flux derived from satellite data. *Journal of Geophysical Research: Atmospheres*, 109, D20103.

Fiedler, S., Crueger, T., D'Agostino, R., Peters, K., Becker, T., Leutwyler, D., Paccini, L., Burdanowitz, J., Bühler, S.A., Uribe Cortes, A., Dauhut, T., Dommenget, D., Fraedrich, K., Jungandreas, L., Maher, N., Naumann, A.K., Rugenstein, M., Sakradzija, M., Schmidt, H., Sielmann, F., Stephan, C., Timmreck, C., Zhu, X. and Stevens, B. (2020) Simulated tropical precipitation assessed across three major phases of the coupled model intercomparison project (CMIP). *Monthly Weather Review*, 148, 3653–3680.

Franke, H., Preusse, P. and Giorgetta, M. (2023) PRIMARY DATA for "Changes in tropical gravity waves and the quasi-biennial oscillation in storm-resolving simulations of idealized global warming". https://www.wdc-climate.de/ui/entry?acronym=DKRZ_LTA_081_ds00002.

Fritts, D.C. and Alexander, M.J. (2003) Gravity wave dynamics and effects in the middle atmosphere. *Reviews of Geophysics*, 41, 1003.

Garcia, R.R. and Richter, J.H. (2019) On the momentum budget of the quasi-biennial oscillation in the whole atmosphere community climate model. *Journal of the Atmospheric Sciences*, 76, 69–87.

Garcia, R.R., Smith, A.K., Kinnison, D.E., de la Cámara, A. and Murphy, D.J. (2017) Modification of the gravity wave parameterization in the whole atmosphere community climate model: motivation and results. *Journal of the Atmospheric Sciences*, 74, 275–291.

Gardner, C.S., Hostetler, C.A. and Franke, S.J. (1993) Gravity wave models for the horizontal wave number spectra of atmospheric velocity and density fluctuations. *Journal of Geophysical Research: Atmospheres*, 98, 1035–1049.

Geller, M.A., Zhou, T., Shindell, D., Ruedy, R., Aleinov, I., Nazarenko, L., Tausnev, N.L., Kelley, M., Sun, S., Cheng, Y., Field, R.D. and Faluvegi, G. (2016a) Modeling the QBO–improvements resulting from higher-model vertical resolution. *Journal of Advances in Modeling Earth Systems*, 8, 1092–1105.

Geller, M.A., Zhou, T. and Yuan, W. (2016b) The QBO, gravity waves forced by tropical convection, and ENSO. *Journal of Geophysical Research: Atmospheres*, 121, 8886–8895.

Giorgetta, M.A., Bengtsson, L. and Arpe, K. (1999) An investigation of QBO signals in the east Asian and Indian monsoon in GCM experiments. *Climate Dynamics*, 15, 435–450.

Giorgetta, M.A., Brokopf, R., Crueger, T., Esch, M., Fiedler, S., Helmert, J., Hohenegger, C., Kornblueh, L., Köhler, M., Manzini, E., Mauritsen, T., Nam, C., Raddatz, T., Rast, S., Reinert, D., Sakradzija, M., Schmidt, H., Schneck, R., Schnur, R., Silvers, L., Wan, H., Zängl, G. and Stevens, B. (2018) ICON-A, the atmosphere component of the ICON earth system model: I. model description. *Journal of Advances in Modeling Earth Systems*, 10, 1613–1637.

Giorgetta, M.A. and Doege, M.C. (2005) Sensitivity of the quasi-biennial oscillation to CO_2 doubling. *Geophysical Research Letters*, 32, L08701.

Giorgetta, M.A., Manzini, E., Roeckner, E., Esch, M. and Bengtsson, L. (2006) Climatology and forcing of the quasi-biennial oscillation in the MAECHAM5 model. *Journal of Climate*, 19, 3882–3901.

Giorgetta, M.A., Sawyer, W., Lapillonne, X., Adamidis, P., Alexeev, D., Clément, V., Dietlicher, R., Engels, J.F., Esch, M., Franke, H.,

Frauen, C., Hannah, W.M., Hillman, B.R., Kornblueh, L., Marti, P., Norman, M.R., Pincus, R., Rast, S., Reinert, D., Schnur, R., Schulzweida, U. and Stevens, B. (2022) The ICON-A model for direct QBO simulations on GPUs (version icon-cscs:baf28a514). *Geoscientific Model Development*, 15, 6985–7016.

Hardiman, S.C., Butchart, N. and Calvo, N. (2014) The morphology of the Brewer-Dobson circulation and its response to climate change in CMIP5 simulations. *Quarterly Journal of the Royal Meteorological Society*, 140, 1958–1965.

Hegglin, M., Kinnison, D., Lamarque, J.-F. and Plummer, D. (2016) CCMI ozone in support of CMIP6-version 1.0.

Hersbach, H., Bell, B., Berrisford, P., Hirahara, S., Horányi, A., Muñoz Sabater, J., Nicolas, J., Peubey, C., Radu, R., Schepers, D., Simmons, A., Soci, C., Abdalla, S., Abellan, X., Balsamo, G., Bechtold, P., Biavati, G., Bidlot, J., Bonavita, M., De Chiara, G., Dahlgren, P., Dee, D., Diamantakis, M., Dragani, R., Flemming, J., Forbes, R., Fuentes, M., Geer, A., Haimberger, L., Healy, S., Hogan, R.J., Hólm, E., Janisková, M., Keeley, S., Laloyaux, P., Lopez, P., Lupu, C., Radnoti, G., de Rosnay, P., Rozum, I., Vamborg, F., Villaume, S. and Thépaut, J.-N. (2020) The ERA5 global reanalysis. *Quarterly Journal of the Royal Meteorological Society*, 146, 1999–2049.

Hohenegger, C., Kornblueh, L., Klocke, D., Becker, T., Cioni, G., Engels, J.F., Schulzweida, U. and Stevens, B. (2020) Climate statistics in global simulations of the atmosphere, from 80 to 2.5 km grid spacing. *Journal of the Meteorological Society of Japan. Series II*, 98, 73–91.

Holt, L.A., Alexander, M.J., Coy, L., Molod, A., Putman, W. and Pawson, S. (2016) Tropical waves and the quasi-biennial oscillation in a 7-km global climate simulation. *Journal of the Atmospheric Sciences*, 73, 3771–3783.

Huffman, G., Stocker, E., Bolvin, D., Nelkin, E. and Tan, J. (2019) GPM IMERG Final Precipitation L3 Half Hourly 0.1 degree x 0.1 degree V06. Distributed in netCDF file format by ICDC, CEN, University of Hamburg.

Kang, M.-J. and Chun, H.-Y. (2021) Contributions of equatorial waves and small-scale convective gravity waves to the 2019/20 quasi-biennial oscillation (QBO) disruption. *Atmospheric Chemistry and Physics*, 21, 9839–9857.

Kawatani, Y. and Hamilton, K. (2013) Weakened stratospheric quasi-biennial oscillation driven by increased tropical mean upwelling. *Nature*, 497, 478–481.

Kawatani, Y., Hamilton, K. and Noda, A. (2012) The effects of changes in sea surface temperature and CO_2 concentration on the quasi-biennial oscillation. *Journal of the Atmospheric Sciences*, 69, 1734–1749.

Kawatani, Y., Hamilton, K. and Watanabe, S. (2011) The quasi-biennial oscillation in a double CO_2 climate. *Journal of the Atmospheric Sciences*, 68, 265–283.

Kawatani, Y., Watanabe, S., Sato, K., Dunkerton, T.J., Miyahara, S. and Takahashi, M. (2010b) The roles of equatorial trapped waves and internal inertia-gravity waves in driving the quasi-biennial oscillation. Part II: three-dimensional distribution of wave forcing. *Journal of the Atmospheric Sciences*, 67, 981–997.

Kawatani, Y., Watanabe, S., Sato, K., Dunkerton, T.J., Miyahara, S. and Takahashi, M. (2010a) The roles of equatorial trapped waves and internal inertia-gravity waves in driving the quasi-biennial oscillation. Part I: zonal mean wave forcing. *Journal of the Atmospheric Sciences*, 67, 963–980.

Klemp, J.B., Dudhia, J. and Hassiotis, A.D. (2008) An upper gravity-wave absorbing layer for NWP applications. *Monthly Weather Review*, 136, 3987–4004.

Lane, T.P. and Knievel, J.C. (2005) Some effects of model resolution on simulated gravity waves generated by deep, mesoscale convection. *Journal of the Atmospheric Sciences*, 62, 3408–3419.

Lehmann, C.I., Kim, Y.-H., Preusse, P., Chun, H.-Y., Ern, M. and Kim, S.-Y. (2012) Consistency between Fourier transform and small-volume few-wave decomposition for spectral and spatial variability of gravity waves above a typhoon. *Atmospheric Measurement Techniques*, 5, 1637–1651.

Leuenberger, D., Koller, M., Fuhrer, O. and Schär, C. (2010) A generalization of the SLEVE vertical coordinate. *Monthly Weather Review*, 138, 3683–3689.

Mauritsen, T., Svensson, G., Zilitinkevich, S.S., Esau, I., Enger, L. and Grisogono, B. (2007) A Total turbulent energy closure model for neutrally and stably stratified atmospheric boundary layers. *Journal of the Atmospheric Sciences*, 64, 4113–4126.

Meinshausen, M., Vogel, E., Nauels, A., Lorbacher, K., Meinshausen, N., Etheridge, D.M., Fraser, P.J., Montzka, S.A., Rayner, P.J., Trudinger, C.M., Krummel, P.B., Beyerle, U., Canadell, J.G., Daniel, J.S., Enting, I.G., Law, R.M., Lunder, C.R., O'Doherty, S., Prinn, R.G., Reimann, S., Rubino, M., Velders, G.J.M., Vollmer, M.K., Wang, R.H.J. and Weiss, R. (2017) Historical greenhouse gas concentrations for climate modelling (CMIP6). *Geoscientific Model Development*, 10, 2057–2116.

Morfa, Y.A. and Stephan, C.C. (2023) The relationship between horizontal and vertical velocity wavenumber spectra in global storm-resolving simulations. *Journal of the Atmospheric Sciences*, 80, 1087–1105.

MPI-M. (2023) Code availability. https://mpimet.mpg.de/en/research/modeling.

Müller, S.K., Manzini, E., Giorgetta, M., Sato, K. and Nasuno, T. (2018) Convectively generated gravity waves in high resolution models of tropical dynamics. *Journal of Advances in Modeling Earth Systems*, 10, 2564–2588.

Nastrom, G.D. and Gage, K.S. (1985) A climatology of atmospheric wavenumber spectra of wind and temperature observed by commercial aircraft. *Journal of the Atmospheric Sciences*, 42, 950–960.

NOAA. (2022) Monthly Global Climate Report for Annual 2021. https://www.ncei.noaa.gov/access/monitoring/monthly-report/global/202113.

Orr, A., Bechtold, P., Scinocca, J., Ern, M. and Janiskova, M. (2010) Improved middle atmosphere climate and forecasts in the ECMWF model through a nonorographic gravity wave drag parameterization. *Journal of Climate*, 23, 5905–5926.

Osprey, S.M., Butchart, N., Knight, J.R., Scaife, A.A., Hamilton, K., Anstey, J.A., Schenzinger, V. and Zhang, C. (2016) An unexpected disruption of the atmospheric quasi-biennial oscillation. *Science*, 353, 1424–1427.

Pahlavan, H.A., Fu, Q., Wallace, J.M. and Kiladis, G.N. (2021) Revisiting the quasi-biennial oscillation as seen in ERA5. Part I: description and momentum budget. *Journal of the Atmospheric Sciences*, 78, 673–691.

Pincus, R., Mlawer, E.J. and Delamere, J.S. (2019) Balancing accuracy, efficiency, and flexibility in radiation calculations for dynamical models. *Journal of Advances in Modeling Earth Systems*, 11, 3074–3089.

Pithan, F., Angevine, W. and Mauritsen, T. (2015) Improving a global model from the boundary layer: total turbulent energy and the

neutral limit Prandtl number. *Journal of Advances in Modeling Earth Systems*, 7, 791–805.

Polichtchouk, I., Wedi, N. and Kim, Y.-H. (2021) Resolved gravity waves in the tropical stratosphere: impact of horizontal resolution and deep convection parametrization. *Quarterly Journal of the Royal Meteorological Society*, 148, 233–251.

Richter, J.H., Butchart, N., Kawatani, Y., Bushell, A.C., Holt, L., Serva, F., Anstey, J., Simpson, I.R., Osprey, S., Hamilton, K., Braesicke, P., Cagnazzo, C., Chen, C.-C., Garcia, R.R., Gray, L.J., Kerzenmacher, T., Lott, F., McLandress, C., Naoe, H., Scinocca, J., Stockdale, T.N., Versick, S., Watanabe, S., Yoshida, K. and Yukimoto, S. (2020) Response of the quasi-biennial oscillation to a warming climate in global climate models. *Quarterly Journal of the Royal Meteorological Society*, 148, 1490–1518.

Salby, M.L. and Garcia, R.R. (1987) Transient response to localized episodic heating in the tropics. Part I: excitation and short-time near-Field behavior. *Journal of Atmospheric Sciences*, 44, 458–498.

Saravanan, R. (1990) A multiwave model of the quasi-biennial oscillation. *Journal of Atmospheric Sciences*, 47, 2465–2474.

Savitzky, A. and Golay, M.J. (1964) Smoothing and differentiation of data by simplified least squares procedures. *Analytical Chemistry*, 36, 1627–1639.

Schirber, S., Manzini, E., Krismer, T. and Giorgetta, M. (2015) The quasi-biennial oscillation in a warmer climate: sensitivity to different gravity wave parameterizations. *Climate Dynamics*, 45, 825–836.

Shepherd, T.G. and McLandress, C. (2011) A robust mechanism for strengthening of the Brewer-Dobson circulation in response to climate change: critical-layer control of subtropical wave breaking. *Journal of the Atmospheric Sciences*, 68, 784–797.

Shepherd, T.G., Plumb, R.A. and Wofsy, S.C. (2005) Preface to J. Atmos. Sci. Special issue on the Antarctic stratospheric sudden warming and split ozone hole of 2002. *Journal of the Atmospheric Sciences*, 62, 565–566.

Skamarock, W.C. (2004) Evaluating mesoscale NWP models using kinetic energy spectra. *Monthly Weather Review*, 132, 3019–3032.

Skamarock, W.C., Park, S.H., Klemp, J.B. and Snyder, C. (2014) Atmospheric kinetic energy spectra from global high-resolution nonhydrostatic simulations. *Journal of the Atmospheric Sciences*, 71, 4369–4381.

Son, S.-W., Lim, Y., Yoo, C., Hendon, H.H. and Kim, J. (2017) Stratospheric control of the madden-Julian oscillation. *Journal of Climate*, 30, 1909–1922.

Stephan, C.C., Strube, C., Klocke, D., Ern, M., Hoffmann, L., Preusse, P. and Schmidt, H. (2019a) Gravity waves in global high-resolution simulations with explicit and parameterized convection. *Journal of Geophysical Research: Atmospheres*, 124, 4446–4459.

Stephan, C.C., Strube, C., Klocke, D., Ern, M., Hoffmann, L., Preusse, P. and Schmidt, H. (2019b) Intercomparison of gravity waves in global convection-permitting models. *Journal of the Atmospheric Sciences*, 76, 2739–2759.

Stevens, B., Satoh, M., Auger, L., Biercamp, J., Bretherton, C.S., Chen, X., Düben, P., Judt, F., Khairoutdinov, M., Klocke, D., Kodama, C., Kornblueh, L., Lin, S.-J., Neumann, P., Putman, W.M., Röber, N., Shibuya, R., Vanniere, B., Vidale, P.L., Wedi, N. and Zhou, L. (2019) DYAMOND: the DYnamics of the atmospheric general circulation Modeled on non-hydrostatic domains. *Progress in Earth and Planetary Science*, 6, 61.

Strube, C., Ern, M., Preusse, P. and Riese, M. (2020) Removing spurious inertial instability signals from gravity wave temperature perturbations using spectral filtering methods. *Atmospheric Measurement Techniques*, 13, 4927–4945.

Terasaki, K., Tanaka, H.L. and Satoh, M. (2009) Characteristics of the kinetic energy Spectrum of NICAM model atmosphere. *SOLA*, 5, 180–183.

Tian, B. and Dong, X. (2020) The double-ITCZ bias in CMIP3, CMIP5, and CMIP6 models based on annual mean precipitation. *Geophysical Research Letters*, 47, E2020GL087232.

Vincent, R.A. and Alexander, J.M. (2000) Gravity waves in the tropical lower stratosphere: an observational study of seasonal and interannual variability. *Journal of Geophysical Research: Atmospheres*, 105, 17971–17982.

Wan, H., Giorgetta, M.A., Zängl, G., Restelli, M., Majewski, D., Bonaventura, L., Fröhlich, K., Reinert, D., Rípodas, P., Kornblueh, L. and Förstner, J. (2013) The ICON-1.2 hydrostatic atmospheric dynamical core on triangular grids-part 1: formulation and performance of the baseline version. *Geoscientific Model Development*, 6, 735–763.

Watanabe, S. and Kawatani, Y. (2012) Sensitivity of the QBO to mean tropical upwelling under a changing climate simulated with an earth system model. *Journal of the Meteorological Society of Japan*, 90A, 351–360.

Watanabe, S., Nagashima, T. and Emori, S. (2005) Impact of global warming on gravity wave momentum flux in the lower stratosphere. *SOLA*, 1, 189–192.

Yao, W. and Jablonowski, C. (2015) Idealized quasi-biennial oscillations in an Ensemble of dry GCM dynamical cores. *Journal of the Atmospheric Sciences*, 72, 2201–2226.

Yoo, C. and Son, S.-W. (2016) Modulation of the boreal wintertime madden-Julian oscillation by the stratospheric quasi-biennial oscillation. *Geophysical Research Letters*, 43, 1392–1398.

Zängl, G., Reinert, D., Rípodas, P. and Baldauf, M. (2015) The ICON (ICOsahedral non-hydrostatic) modelling framework of DWD and MPI-M: description of the non-hydrostatic dynamical core. *Quarterly Journal of the Royal Meteorological Society*, 141, 563–579.

SUPPORTING INFORMATION

Additional supporting information can be found online in the Supporting Information section at the end of this article.

How to cite this article: Franke, H., Preusse, P. & Giorgetta, M. (2023) Changes of tropical gravity waves and the quasi-biennial oscillation in storm-resolving simulations of idealized global warming. *Quarterly Journal of the Royal Meteorological Society*, 149(756), 2838–2860. Available from: https://doi.org/10.1002/qj.4534